Frequent resuspension of glaciomarine coastal sediments as an important source of iron to the West Antarctic Peninsula

Rhiannon L. Jones[1,2]*, Maeve C. Lohan[2], Tobias Ehmen[3], Lisa Friberg[4], Ben Lincoln[5], Katy Sheen[6], Siobhan Foden[1], Katrien Van Landeghem[5], Kate Retallick[5], George Dadd[7], James Scourse[6], Amber L. Annett[2]

[1]British Antarctic Survey, Cambridge, UK
[2]School of Ocean and Earth Science, University of Southampton, Southampton, UK
[3]Bjerknes Centre for Climate Research, University of Bergen, Norway
[4]School of Earth Sciences, University of Bristol, UK
[5]School of Ocean Sciences, Bangor University, UK
[6]Earth and Environmental Science, University of Exeter
[7]Kiote Ltd, UK

Correspondence to: Rhiannon L. Jones (rhines@bas.ac.uk)

Abstract. Southern Ocean primary productivity is often limited by the availability of the essential micronutrient iron (Fe), and sediment-derived fluxes of Fe from the Antarctic shelf have been linked with hotspots of productivity. Glacial meltwater along the West Antarctic Peninsula delivers significant volumes of Fe-rich glacially weathered material to shelf surface sediments. Measured acoustic doppler current profiler and acoustic backscatter turbidity data indicate ongoing resuspension of sediment in the coastal region. Onboard mesocosm experiments simulated resuspension of oxic sediments, rich in highly reactive Fe (2 – 9 mg g^{-1}), in the nearshore glaciated West Antarctic Peninsula across King George Island, Anvers Island, and Adelaide Island. These experiments produced a high sustained bottom water enrichment in dissolved Fe of ~4 – 12 nM over the 48h experiment duration.

Our observations support a dissolved Fe flux to the water column of 0.18 – 4.0 µmol m^{-2} d^{-1} by resuspension within the glaciated fjords, demonstrating that resuspension of reactive oxic nearshore sediments is a key source of dissolved and reactive particulate Fe to Antarctic shelf waters, the export of which could potentially supply bioavailable Fe to Fe-limited Southern Ocean waters.

1 Introduction

Iron (Fe) is an essential micronutrient for primary producers, yet availability is generally low in the surface ocean, and seasonal Fe limitation of primary production is observed globally, including across much of the Southern Ocean (Browning & Moore, 2023; Liu & Millero, 2002; Von Der Heyden et al., 2014). Therefore, Fe availability is a bottom-up driver of food web productivity and carbon cycling, and is a key modulator of climate both in the present day and over glacial-interglacial timescales (Martin, 1990).

Dissolved Fe (dFe) can be operationally defined as soluble Fe (< 0.02 μm) and colloidal/nanoparticulate (0.02 – 0.2 μm) Fe (sFe and cFe, respectively). Soluble (or truly dissolved) Fe is the most bioavailable form, but is rapidly oxidised to Fe(III) and precipitated unless stabilised by organic colloids (Lam et al., 2012), although this oxidation rate can be slowed in cold environments (e.g. Dold et al., 2013). The colloidal Fe phase (~0.02 – 0.2 μm) typically accounts for half or more of marine dFe, as ligand-bound Fe, or nanoparticles of ferrihydrite, goethite, and other Fe (oxyhydr)oxides, ranging in solubility and bioavailability (Kunde et al., 2019; Raiswell & Canfield, 2012).

Glaciers and ice sheets in high latitude environments deliver high volumes of sediment enriched in reactive or bioavailable Fe, and other bioactive elements to the continental shelf (Ardelan et al., 2010; Chinni et al., 2026; Ebner et al., 2026; Hawkings et al., 2017; Hawkings et al., 2014; Laufer-Meiser et al., 2021). Glacial meltwater comprises a significant, potentially bioavailable, (nano)particulate Fe component (Fourquez et al., 2023; Hawkings et al., 2014; Jones et al., 2025; Monien et al., 2017; Schroth et al., 2009; Zhang et al., 2015), or a bioavailable reduced Fe (Fe(II)) component (Chinni et al., 2026; Dold et al., 2013). Hawkings et al. (2014) estimate global bioavailable Fe fluxes from glacial runoff of 0.4 – 2.54 Tg yr^{-1} and 0.06 – 0.17 Tg yr^{-1} from Greenland and Antarctica, respectively.

During the melt season, sediment-laden meltwater plumes spread across fjords and bays, delivering material to the seafloor according to particle properties and the hydrodynamic regime (Meslard et al., 2018). Glacially-derived particulate and colloidal Fe may therefore significantly influence the bioavailable Fe supply to polar shelf sediments and accelerating melt rates across the high latitudes are expected to alter the delivery of terrestrial Fe to the ocean.

High latitude continental shelves supply an important benthic input of Fe to the water column (Elrod et al., 2004), evidenced by sediment-derived Fe enrichment in shelf waters (Sherrell et al., 2018; Tonnard et al., 2020), and by direct measurements of benthic Fe mobilisation (Burdige & Christensen, 2022). However, the magnitude, distribution, and pathways of shelf-derived benthic Fe fluxes remain poorly constrained, particularly in remote regions such as the Antarctic (De Jong et al., 2012; Monien et al., 2014; Sherrell et al., 2018).

Sediment resuspension occurs through hydrodynamic forcing; internal waves, ocean eddies, tides and currents act to resuspend particles above the sediment-water interface (De Jonge & Van Beuselom, 1992; Gargett et al., 2004). In the northern WAP, strong winds drive vertical mixing, and sediment tracers show vigorous benthic exchange at Marian Cove, transporting suspended particles and sediment-derived solutes into bottom waters (Jones et al., 2023; Meredith et al., 2018; Schloss et al., 1997). Bown et al. (2018) show that turbidity increases in the deeper layers with proximity to the coast, from the WAP shelf to Ryder Bay (near the Sheldon Cove sediment core site) and Scott et al. (2021) show wind-driven reversals of bottom water flow directions in Ryder Bay over an 8-day period, inducing across-shelf exchange and mixing of water masses.

Through resuspension, nutrients such as Fe can be released to the water column. Upwelling or direct input to the mixed layer can make this Fe available to primary producers (De Jong et al., 2015; Nielsdóttir et al., 2012). Across the West Antarctic Peninsula (WAP) shelf, the frequency, spatial influence, and persistence of sediment resuspension events remain poorly quantified. In glaciated fjords, sediment can re-enter the water column via turbulent mixing over glacial sills (Meredith et al.,

2022; Venables et al., 2013), or through entrainment of deep water and sediment by buoyant meltwater, as observed in Jones et al. (2023), both driven by meltwater-ambient water interactions.

This study investigates the behaviour and reactivity of glaciomarine sediment Fe along the coastal West Antarctic Peninsula. Incubation experiments conducted onboard the *RRS James Clark Ross* in January 2020 involved adding surface sediments to bottom waters from the same locations to quantify the reactive Fe release during sediment resuspension. We compare changes in dissolved and truly dissolved Fe with the solid phase and pore water properties of the added surface sediments. Combined with evidence of physical mixing of sediment at each site, we seek to quantify the release of reactive and dissolved Fe to the water column during resuspension of Antarctic glaciomarine coastal sediments.

2 Physical setting

Accelerating glacier retreat is observed across the WAP, driven by oceanic and atmospheric warming (Cook et al., 2016). In the south, warm incursions of modified Circumpolar Deep Water drive basal retreat of glacier grounding lines, contrasting with the north, where atmospheric temperatures drive surface ice shelf thinning and melting through surface runoff (Cook et al., 2016; Rignot et al., 2004).

Samples were collected onboard the *RRS James Clark Ross* during the JR19002 Icebergs 3 expedition (January 2020), from three glaciated island bays along the WAP coast: King George Island, Anvers Island, and Adelaide Island (Figure 1, Table 1) (Scourse et al., 2020). A subsection of the echosounder (EK80) data was collected during the *RRS James Clark Ross* JR18003

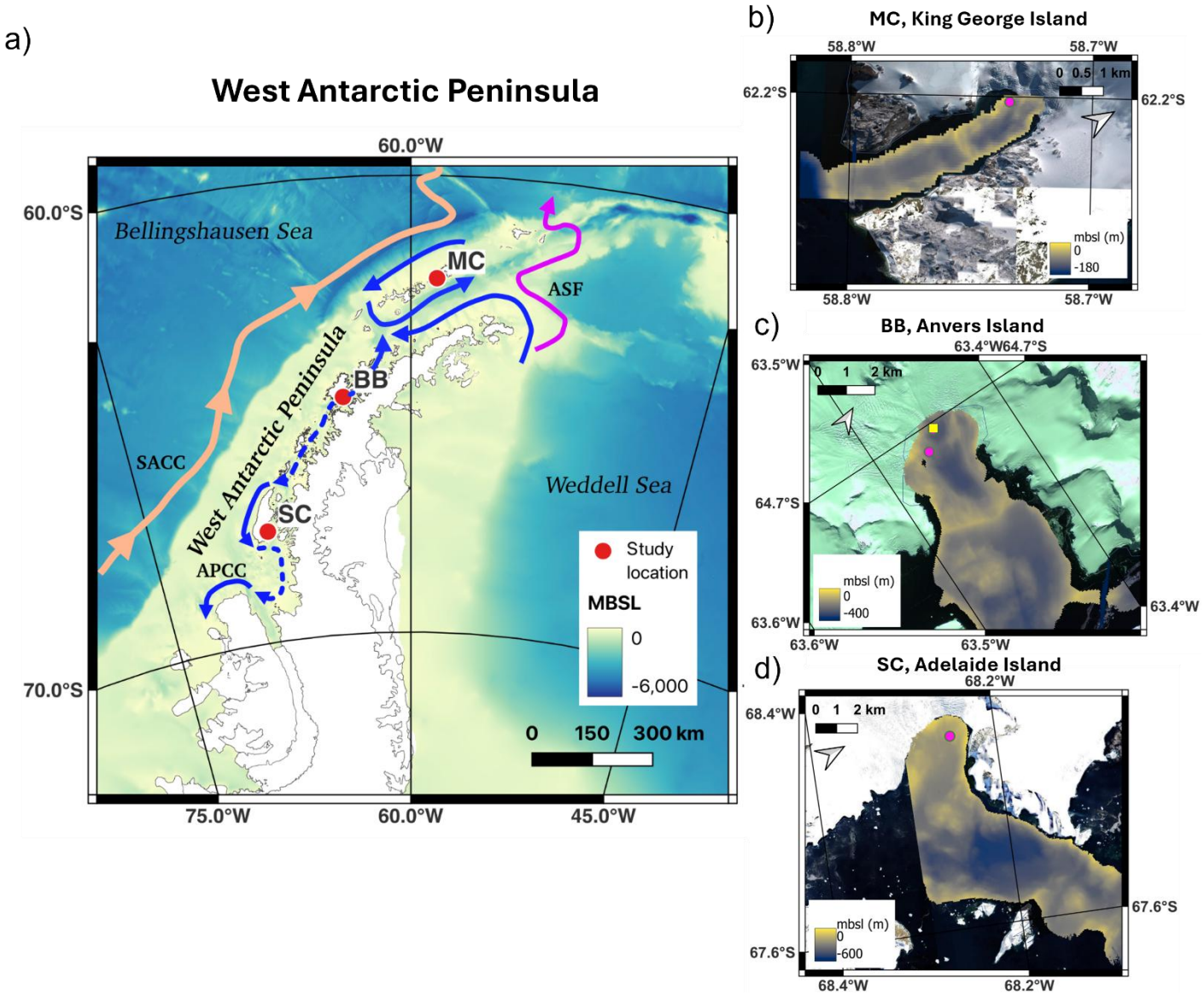

Figure 1: a) Study location map of the West Antarctic Peninsula, annotated with the main influencing currents and study sites. Abbreviations MC stands for Marian Cove, King George Island; BB for Börgen Bay, Anvers Island; and SC for Sheldon Cove, Adelaide Island. Currents ASF = Antarctic Subpolar Front; APCC = Antarctic Peninsula Coastal Current; SACC = Southern Antarctic Circumpolar Current Front. Regional maps of b) Marian Cove, c) Börgen Bay and d) Sheldon Cove are presented with the coring sites annotated in pink, overlaying contemporaneous multibeam bathymetry data (e.g. Jones et al., 2023). Google Earth Satellite as basemap. Imagery © Google. Multibeam bathymetry data in b) – d) was collected during the sampling period (Retallick et al. 2021).

Icebergs 2 expedition (December 2017) to the same glaciated bays (Sands et al., 2019). In Sheldon Cove, Ryder Bay, Adelaide Island, sampling was conducted approximately 1 km from the marine-terminating Sheldon Glacier grounding line (site SC). Sampling at the central site, Börgen Bay, Anvers Island (site BB), was approximately 1.2 km from the marine-terminating William Glacier grounding line. The northernmost site (MC) was in Marian Cove, Maxwell Bay, King George Island, approximately 750 m from the land-terminating Fourcade Glacier grounding line. Study site location and sampling depth is provided in Table 1 and shown in Figure 1. Oceanographic properties of each site are published in Jones et al. (2023) and Scourse et al. (2022).

Stable oxygen and radiogenic radium isotope data indicate that sediment-laden surface run-off and glacier melt from the coast is evident across these bays, with evidence of cross-shelf transport of glacially sourced material (Annett et al., 2017; Jones et al., 2025; Jones et al., 2023; Meredith et al., 2017). Estimates of sedimentation rates in these regions at the time of sampling are 0.5 cm yr^{-1}, 0.17 cm yr^{-1}, and 0.11 cm yr^{-1} in Marian Cove, Börgen Bay, and Sheldon Cove, respectively (James Scourse, personal comms.).

3 Methods

3.1 Sediment and seawater sampling at the West Antarctic Peninsula

Sediment core samples were collected using core tubes mounted onto an Oktopus Multicorer (MUC), Oktopus GmbH. For sediment-water incubation experiments, pristine cores were selected based on a visually inspected undisturbed and horizontal sediment-bottom water interface, and > 10 cm of sediment.

Sediment incubation water was collected from the CTD rosette, pooled from 3, 24 L Niskins fired at the same depth, ~10 - 12 m above the seafloor. Seawater was collected into 20 L carboys (Nalgene), through 0.2 µm filter cartridges (AcroPak™ 300 PTFE, Pall) to remove large biological material and particulate material. The filter and carboys were rinsed 3 times with ~1 L of seawater prior to collection. All plasticware and tubing used to collect seawater was acid-cleaned with 10% HCl (ROMIL-SpA™). Carboys were kept in the dark and stored at 4 °C before and during the incubation. Bottom water at Börgen Bay was from approximately 770 m away from the coring site due to issues with core recovery, which is representative of overlying waters considering the proximity. The CTD rosette and Niskins used for bottom water collection were not trace metal clean, although handling was done with particle free gloves and minimal exposure to air to reduce potential contamination.

Table 1: Sample location and depth for seawater and sediment from the West Antarctic Peninsula

Station	Parameter	Sheldon Cove, Adelaide Island	Börgen Bay, Anvers Island	Marian Cove, King George Island
Water collection	Latitude	67.5196° S	64.7036° S	62.2010° S
	Longitude	68.2487° W	63.4522° W	58.7343° W
	Bottom depth (m)	187	264	79
	Sample depth (m)	178	254	67
Sediment collection	Latitude	67.5190° S	64.7071° S	62.2014° S
	Longitude	68.2495° W	63.4627° W	58.7319° W
	Sample depth (m)	191	200	101

3.2 Sediment and pore water sampling

Sediment cores for pore water and solid phase parameters were collected from cores from the same MUC deployment. Cores collected were either sectioned for porosity analysis or sampled for pore waters using Rhizons (Seeberg-Elverfeldt et al., 2005). Samples for porosity analysis were placed into Ziploc bags and frozen immediately at -20 °C. For pore waters, Rhizon samplers (Rhizosphere) of filter size ~0.18 µm were inserted through pre-drilled holes at 0.5 – 1 cm intervals down-core. An acid-clean 20 mL syringe was secured to the end of each Rhizon, and a block was inserted between syringe and plunger to apply and maintain suction. A small volume (< 1 mL) of initial filtrate was used to rinse the Rhizon and syringe. Separate cores were collected for nitrate and dissolved metals. For dissolved metal analysis, pore waters were collected into 15 mL LDPE Nalgene bottles and acidified with 1 µL mL^{-1} of HCl (ROMIL-UpA™). Nitrate samples were collected into HDPE Nalgene bottles and immediately frozen at -20 °C onboard.

Separate cores were also collected for oxygen determination. Cores were transported to a temperature-controlled laboratory at 4 °C and fitted with a Pyro Science FireSting O_2-Mini sensor connected to a laptop with Oxygen Logger software. The probe was attached to a core lid to avoid atmosphere-water gas exchange and moved between the base and top of the core to take measurements. Ten to 20 consecutive measurements were made at every 0.5 cm in the sediment in two cores, which were averaged to calculate O_2 concentrations (µmol L^{-1}). The nitrate and oxygen data is presented in Friberg et al. (2026).

3.3 Incubation experiment set-up

For the sediment incubations, the top 0.5 cm of each core was collected. The sediment was mixed to homogenise the material, and then 25 – 30 mL of sediment was transferred into three carboys containing corresponding bottom water. The fourth, non-sediment addition carboy represents the experiment control. Remaining sediment was immediately frozen at -20 °C. Carboy

lids were kept loose to allow for atmosphere-water gas exchange to avoid reducing conditions during the incubation. One hour prior to subsampling, carboys were mixed vigorously for one minute to mimic energetic resuspension.

3.3.1 Incubation sampling

Samples for trace metal analysis were collected at the following time points: 0 (prior to), 1, 4, 12, 24, 36 and 48 h after sediment addition (T0, T1, T4, T12, T24, T36 and T48 hereafter) in-line, using acid-cleaned tubing and a peristaltic pump. LDPE Nalgene bottles were used for total dissolvable and soluble metals (60 mL) and for dissolved metals (125 mL), pre-cleaned according to GEOTRACES protocols (Cutter et al., 2017). All sample bottles were rinsed three times with subsample before filling. For total dissolvable iron (TdFe) and manganese (TdMn), samples were collected unfiltered. Dissolved Fe (dFe) samples were collected similarly, with an added in-line filtration through an 0.2 µm AcroPak™ 300 PTFE filter (Pall), rinsed with sample water. A sequential ultra-filtration step was performed to sample the soluble fraction (sFe, <0.02 µm). Detailed ultrafiltration methodology is given in the Supplementary Material. Filtered dFe subsamples were taken to a class-100 clean bubble built onboard the ship to perform ultra-filtration, following Ussher et al. (2010) and all dFe and sFe samples were acidified with 10N HCl (ROMIL-UpA™) to a pH of 1.8 for flow injection analysis; tdM samples were acidified with 10 N HCl (ROMIL-UpA™) to 1 mL L^{-1} for quantification using High Resolution Inductively Coupled Plasma – Mass Spectrometry (Thermo ELEMENT 2XR).

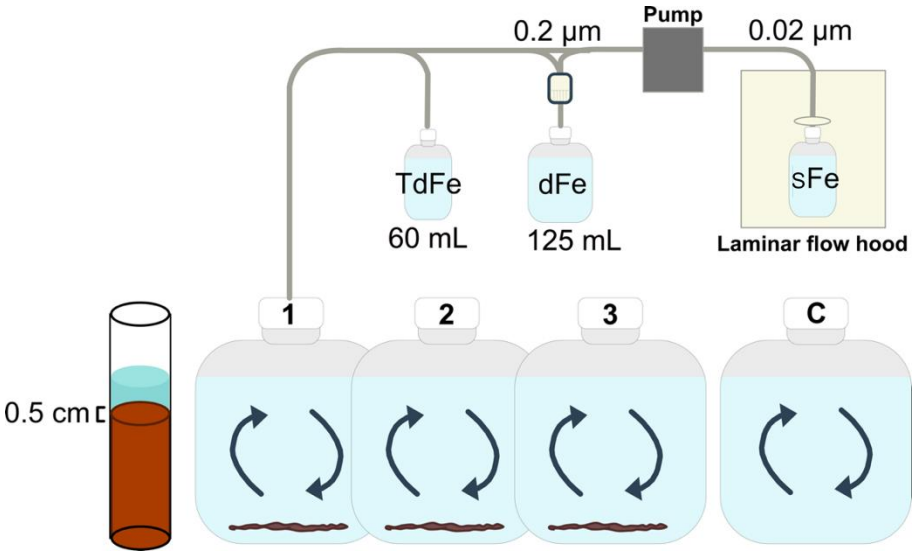

Figure 2: Incubation experimental set-up. The top 0.5 cm of sediment was added to three replicates of 20 L, with one control carboy. Carboys were shaken an hour prior to every subsampling timepoint.

3.3.2 Determination of dissolved iron concentration

The dFe and sFe concentrations were determined using Flow Injection – Chemiluminescence (FI-CL) (Bowie & Lohan, 2009; Obata et al., 1993). Analysis was conducted inside a class-1000 clean air laboratory at the National Oceanography Centre, Southampton, UK. Iron concentration quantification was performed using standard addition to low Fe seawater. For high Fe samples, a calibration curve of 0 – 200 nM or 0 – 20 nM was conducted. Sample precision was determined using certified reference material NASS-6 (National Research Council, Canada; 8.86 ± 0.82 nM) measuring 8.58 ± 0.43 nM (± 1 s.d.) by standard addition, and internal standard DY021, measuring 1.14 ± 0.15 nM (n = 13) (± 1 s.d.) for repeat measurements, respectively. For low Fe samples, a calibration curve of 0 – 1 nM and 0 – 2 nM was conducted, with internal standards ZIPLOC I and ZIPLOC II measuring 0.38 ± 0.038 nM (n = 18) and 0.15 ± 0.02 nM (n = 7) for repeat measurements, respectively. Sample measurements with an uncertainty (1 s.d.) of > 5 % were discarded and repeated. Detailed methodology is given in the Supplementary Material.

3.3.3 Determination of total dissolvable and pore water metals

Incubation total dissolvable metals and pore water metals were analysed using a Thermo Scientific™ ELEMENT HR-ICP-MS at the University of Southampton or University of Bristol. Concentrations of Fe and manganese (Mn) were determined using a gravimetrically prepared multi-element standard, a five-point calibration curve and blanks. Samples and calibrants were diluted in 0.3 M distilled HNO_3 under class-100 clean lab conditions. The limit of detection (3 × blank s.d.) for Fe was 0.084 µM, and for Mn was 0.244 µM. No reference material in seawater matrix was available with a concentration high enough to be within the targeted calibration range. Sample precision was therefore validated using the river water SLRS-4 reference material for total dissolvable Fe (National Research Council, Canada; Fe = 103 ± 5 µg L^{-1}, measured value = 107 ± 10 ug L^{-1}) and BIR-1 for pore waters (Reykjavik Iceland Basalt). The RSD (1σ) ranged between 3.6% to 9.3% and averaged 6.2% for repeat measurements of BIR-1 across all elements (n=8) (Friberg et al. 2026).

3.4 Estimating incubation pore water concentrations

Porosity was calculated as the difference between the total wet weight and total dry weight of sediment, assuming the density of seawater, density of salt-free sediment, and the density of salt were 1 g cm^{-2}, 2.6 g cm^{-2}, and 2.165 g cm^{-2} respectively. The salinity of the seawater was 31 PSU. The final volumes of water, sediment and salt were derived to find:

$$\Phi = \frac{V_{water}}{V_{water} + V_{sed} + V_{salt}} \times 100 \quad (1)$$

It is possible to estimate the required pore water [dFe] concentration that would account for the observed maximum increase in [dFe] within the incubations. Using the measured sediment porosity (ø), the total pore water addition per L of bottom water (V_{PW}) can be calculated as

$$V_{PW} = \emptyset \times \frac{V_S}{V_E} \quad (2)$$

Where V_S is the total volume of sediment added, and V_E is the total experiment volume. Using the maximum ΔdFe for each station as the addition of dFe, the pore water concentration required to account for the total increase in [dFe] ($[dFe]_P$) can be calculated as:

$$[dFe]_P = \frac{\Delta dFe \times V_E}{V_S \times \Phi} \quad (3)$$

3.5 Sediment characteristics

3.5.1 Sediment reactive iron extraction

Sediment iron speciation was determined using a modified sequential extraction procedure (Poulton and Canfield, 2005). The procedure is designed to quantify the operationally defined most reactive Fe oxide (Fe_{ox1}), such as lepidocrocite or ferrihydrite; easily reducible Fe(II) (Fe_{HCl}) fractions, such as acid volatile iron monosulfides or unsulfidised Fe(II); and the less reactive Fe oxide fraction (Fe_{ox2}). The surface sediments retained from sediment incubation experiments were left to thaw briefly, then weighed out into acid-clean 15 mL centrifuge tubes to approximately 60 mg dry weight equivalent and treated with 10 mL 0.5 M HCl (ROMIL-SpA™). Samples were placed on a shaker table to react for 1 h before centrifugation at 4000 rpm for 4 min. To measure the unsulfidised Fe(II) component (Fe_{HCl}), a total of 250 µL of sample supernatant was added to 10 mL of a 0.05 M HEPES and 0.2 g L^{-1} ferrozine solution and left to react for 15 min (Viollier et al., 2000). The Fe(II) concentration of this solution was measured using a spectrophotometer set to 563 nm, against stock standard solutions (0 – 40 ppm). To measure the highly reactive Fe oxide fraction (Fe_{ox1}), the remaining supernatant was retained for Inductively Coupled Plasma Optical Emission Spectroscopy (ICP-OES) analysis (see below).

A second subsample of 250 mg dry weight equivalent wet sediment was weighed out and treated using a citrate-bicarbonate-dithionite (CBD) extraction (Fisher et al., 2021). Each sample was treated with 13 mL of 0.11 M sodium bicarbonate ($NaHCO_3$), and 0.27M trisodium citrate $Na_3C_6H_5O_7 \cdot H_2O$ and placed in a water bath at 80 ˚C for approximately 15 min. Sodium dithionite (0.25 g) was then dissolved in 2 mL of 0.11 M $NaHCO_3$ and 0.27 M $Na_3C_6H_5O_7 \cdot H_2O$ and added to each sample. The solution was agitated and then heated at 80 ˚C for a further 15 min. Samples were centrifuged at 4000 rpm (10 min) and the supernatant removed and acidified to pH < 2 using 12 M HCl (ROMIL-SpA™), to avoid precipitation of Fe(III). Samples

were then filtered through 0.2 µm filters (PES, Acropak) and stored for ICP-OES analysis to find the total Fe_{ox2} component. This primarily solubilizes more crystalline, less reactive iron oxides such as goethite and hematite. Some magnetite and an Fe(III)-rich smectite clay (nontronite) may also be dissolved here (Hepburn et al., 2020; Poulton & Canfield, 2005; Slotznick et al., 2020).

The supernatants from both extractions were diluted 70-fold in 2% HNO_3 (twice distilled in-house in PTFE vessels) and analysed by inductively coupled plasma - optical emission spectrometry. Accuracy was validated against a standard calibration using gravimetrically prepared standards of known concentration. Replicates were better than 9% (1 s.d.). All solid-phase extraction iron data are presented in the Supplementary Dataset. Across the three leaches, two out of three sediments were run in duplicate and the standard deviation for Fe concentration was < 10%. Method blanks measured < 20 ppb or < 0.05 % of the mean Fe conc.

3.5.2 Scanning Electron Microscopy of incubation sediments

The mineralogical composition of sediments was analysed using Scanning Electron Microscopy - Electron Dispersive X-ray Spectroscopy (SEM-EDS). Briefly, samples were thawed and oven-dried, before being placed in resin and polished using diamond grinders to produce a flat smooth surface. The retained sediments samples (n=3) were studied using a Carl Zeiss Leo 1450VP SEM equipped with an Oxford Instruments X-Act 10 mm^2 area SEM-Energy Dispersive Spectrometer. Samples were placed on the stage of the microscope under vacuum conditions of < $1x10^{-4}$ mbar to avoid electrical charging, and analysis was performed at a working distance of 12 – 13 mm, with a voltage of 15 kV. Resolution was approximately 1 µm. The SEM-EDS was calibrated for energy calibration and beam measurement using a cobalt metal standard at 20 kV and a working distance of 15 mm. Chemical and morphological properties of the particles were determined by elemental maps of 50 µm – 1000 µm size. Three maps of each site were created to ensure statistical significance of results. Total bulk elemental composition of each mapped area was determined using the Energy Dispersive Spectrometer and total element wt% is reported. Additionally, maps of individual elements and identified elemental phases were created using AZtec software. Element and phase weight percent are reported as the mean, unless stated otherwise. The specific density of each phase was approximated using the average specific density of the most common mineral form of each phase, obtained from the Mindat database (Mindat.org). This was then used to convert the phase abundance (% of pixels) to phase wt%. The SEM-EDS elemental data is available in the Supplementary Dataset.

3.5.3 Water column suspended particulate material

Water column suspended particulate matter (SPM) was sampled from the CTD rosette for bottom waters (~10 m from the seafloor). Sample water was collected into 5 L jerrycans for a maximum of 15 L at each depth. Seawater was filtered over 47 mm 0.2 µm GF/F Whatman filters that were ashed and weighed prior to the cruise. Filters were washed with 200 mL Milli-Q water to remove salt, and frozen at -20 °C before analysis. Filters were weighed again, then furnaced at 450 °C to distinguish the organic content from the total SPM. Three replicates were taken per water sample with a weighing error of 0.14 – 0.6 %, determined by process blanks. The standard deviation for SPM between sampled replicates ranged from 0.03 to 3.77 mg L^{-1}, with a median standard deviation of 0.38 mg L^{-1}. For organic SPM, the standard deviation between replicates ranged from 0.01 to 0.66 mg L^{-1}, with a median standard deviation of 0.08 mg L^{-1}.

3.6 Water column velocity and echo sounder profiles

Water current velocity and direction was measured using a 75 kHz Teledyne RDI Ocean Surveyor (OS75) VMADCP. Data was acquired using VmDas (v 1.42) and navigation data was taken from the Seatex GPS system. The VMADCP was deployed in narrowband mode with a surface blanking distance of 8 m. When waters were less than 500 m, bottom tracking was enabled and the bin size was set to 8 m, to increase resolution. The number of bins was set to 63. The standard deviation is 30 cm s^{-1} for 8 m bins.

The EK80 wideband echo sounder was used to create images of acoustic backscatter in the water column. Three transducers were installed: a 38 kHz (1 ms pulse), 70 kHz (8 ms or 4 ms pulse) and 120 kHz (1 ms pulse) transducer. Data was collected mostly from the 70 kHz transducer, from 7 – 13 m depth from the surface, with a pulse duration of 8 or 4 ms in most cases. The EK80 was calibrated at the start of the cruise according to Demer et al. (2015). Data was processed and using the python module echopype (v0.10; (Lee et al., 2024)), where noise attenuation was done according to De Robertis and Higginbottom (2007).

4. Results

4.1 Pore water auxiliary parameters

At all sites, bottom waters were well-oxygenated (O_2 > 160 µM), and sediment pore waters were under oxic conditions at 0.5 cm depth, ranging from 37 to 143 µM, with a measured oxygen penetration depth of 3 cm (Table 2). The nitrate penetration depth (where nitrate was < 1 µM) was 3 – 4 cm where measured.

Table 2: Bottom water O_2 concentrations, and sedimentary redox indicators and porosity measurements

Station	Bottom water O_2	Surface sediment O_2	Oxygen penetration depth[a]	Nitrate penetration depth[a,b]	Surface porosity
	µM	*µM*	*cm*	*cm*	-
Sheldon Cove	181	37	3	3	0.644
Börgen Bay[c]	265	105[c]	3	n.m.	0.744
Marian Cove	332	132	3	4	0.746

[a]These are defined as the depths below which the O_2 concentration was < 3 µM and the nitrate concentration was < 1 µM, after Burdige and Christensen (2022).

[b]Nitrate data is published in Friberg et al. (2026).

[c]At Börgen Bay, sediment oxygen and porosity measurements are taken from a different coring site, ~3 km away.

N.m. = not measured.

4.2 Sediment pore water metal concentrations

Sediment pore water concentrations for Fe and manganese (Mn) are given in Figure 6. At 0.25 cm, pore water Fe was 2.7 µM at the Marian Cove site and 1.1 µM at the Sheldon Cove site and generally increased with depth. The highest overall pore water Fe was observed at Marian Cove, where Fe increased rapidly to 21 µM at 0.75 cm depth, and to a maximum of 723 µM at 6 cm depth. Sheldon Cove pore water Fe was also high at shallow depths, peaking at 190 µM at 3.5 cm depth. Sampling difficulties limited sediment acquisition at Börgen Bay, and therefore this station is excluded.

Dissolved Mn between the two WAP sites were comparable. At Marian Cove, Mn ranged from 9.1 µM at 0.25 cm, to a peak of 45.6 µM at 4 cm depth, before moderately decreasing to 28.5 µM at 9 cm depth. Sheldon Cove surface Mn was lower, measuring 3.1 µM at 0.25 cm, but increased to 28.4 µM at 1.5 cm depth.

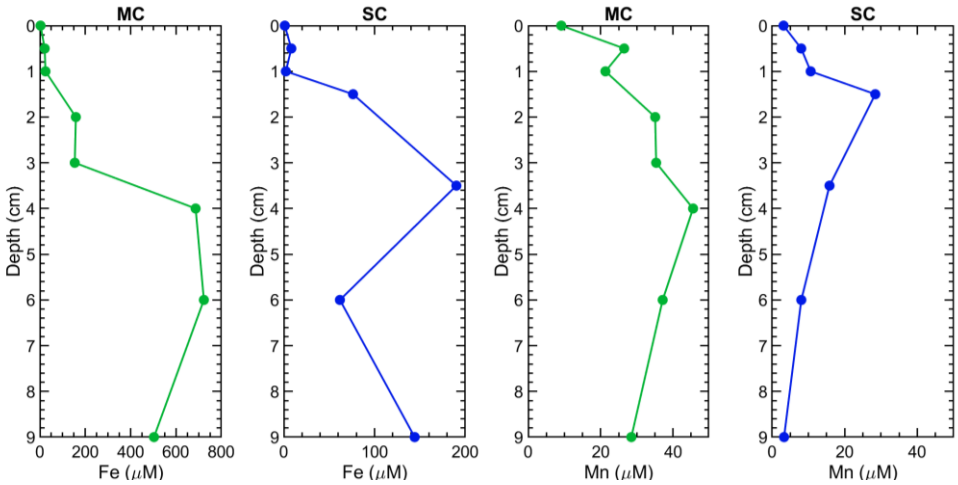

Figure 6: Pore water Fe and Mn profiles for sediment cores from the WAP for a-b) Marian Cove and Sheldon Cove (c-d).

4.3 Solid phase sediment mineralogy

Solid phase elemental composition analysis on coretop (top 0.5 cm) material was conducted using Scanning Electron Microscopy, generally assuming an oxide composition of material. After oxygen, silicon (Si) was the most abundant element (32.0 – 36.6 wt %), followed by aluminium (Al, 9.3 – 11.2 wt %). Marian Cove Fe was highest ($\bar{x} \pm 2\sigma = 5.4 \pm 1.0$ wt %), followed by Börgen Bay (5.2 ± 0.2 wt %) and Sheldon Cove (4.0 ± 1.0 wt %). Based on estimates from Taylor and McLennan (1985), the sites exceeded the upper crustal mean Fe and Al content of 3.5 wt % and 7.6 wt %, respectively (Figure S1). Inter-site Fe and Al wt % exhibited a significant linear correlation ($r^2 = 0.83$). The WAP sites had Fe/Al and Mn/Al ratios of 0.42 –

0.50 and 0.009 – 0.013, respectively. The abundance of Si and Al indicates a high component of silicates, such as sheet silicates and aluminosilicates within the sediments studied.

Elemental phase analysis identified several common and trace phases across sediments, where elements are grouped together based on pixel clustering across the elemental map. The predominant phase at all three sites was rich in Si and Al and accounted for between 47 – 83 % of pixels (median = 75%). In this phase, Si and Al remained reasonably consistent: Si contributed 25.4 ± 0.2 wt% (Marian Cove), 26.5 ± 0.1 wt % (Börgen Bay) and 27.9 ± 0.6 wt% (Sheldon Cove), while Al contributed 12.1 ± 0.1 wt% (Marian Cove), 10.9 ± 0.01 wt% (Börgen Bay) and 10.6 ± 0.8 wt% (Sheldon Cove). This phase also tended to contain Fe (1.5 – 5.1 wt%), as well as a consistent measurable component of Na, Mg, S, Cl, K, Ca, Ti and Mn at concentrations comparable with crustal values (Wedepohl, 1995).

4.4 Leached reactive iron

The absolute contents of highly reactive iron, Fe_{ox1}, in surface sediments were 38 ± 0.8 μmol g^{-1}, 94 ± 0.9 μmol g^{-1} , and 165 ± 15.3 μmol $g^{-}$for SC, BB and MC, respectively, or 5.3 ± 1.0 %, 9.7 ± 1.0 % and 17.7 ± 0.4 % of the total Fe (Section 4.3). The content of less reactive Fe oxides (Fe_{ox2}) was 15.9 ± 1.4 μmol g^{-1}, 48.6, and 126.3 ± 23.9 μmol g^{-1} for SC, BB and MC, respectively, or 2.2 ± 1.0 %, 5.0 ±1.0 %, and 13.5 ± 0.3 % of the total Fe. These two fractions combined are 0.3, 0.8, and 1.6 wt % for SC, BB, and MC respectively, or 7.5 ± 2.0 %, 14.7 ± 2.0 %, and 31.3 ± 0.7 % of the total Fe. The total easily reducible Fe, $Fe(II)_{HCl}$, at each site was 0.006, 0.008 and 0.015 wt% for SC, BB and MC, respectively, or 0.1 – 0.3% of the total Fe.

4.5 Suspended particulate material

Suspended particulate material in the bottom water samples ranged from 1.43 – 1.84 mg L^{-1} in Marian Cove ($\bar{x} = 1.60 \pm 0.27$ mg L^{-1}), 1.00 – 5.68 mg L^{-1} in Börgen Bay ($\bar{x} = 1.84 \pm 1.36$ mg L^{-1}), and 2.69 – 3.79 mg L^{-1} in Sheldon Cove ($\bar{x} = 2.90 \pm 0.45$ mg L^{-1}). Organic SPM ranged from 0.28 – 0.33 mg L^{-1} in Marian Cove ($\bar{x} = 0.29 \pm 0.03$ mg L^{-1}), 0.19 – 1.22 mg L^{-1} in Börgen Bay ($\bar{x} = 0.22 \pm 0.03$ mg L^{-1}), and 0.57 – 0.75 mg L^{-1} ($\bar{x} = 0.58 \pm 0.13$ mg L^{-1}) in Sheldon Cove. Sheldon Cove therefore had the highest mean suspended particulate material, non-organic suspended material, and organic suspended material. Few studies have measured SPM in bottom waters along the WAP coast. Domack et al. (1994) found that the background SPM in Brialmont Cove (Hughes Bay, Graham Land, West Antarctic Peninsula) was 0.8 – 1.0 mg L^{-1}. Furthermore, Leventer and Dunbar (1985) found that SPM in the Bransfield Strait is usually less than 1 mg L^{-1} in surface waters. We therefore suggest that SPM values of > 1 mg L^{-1} are above background. We note that SPM samples were not targeted based on sediment plumes, as determined by EK80/acoustic data, and therefore sediment resuspension signals were not necessarily sampled. However, applying the total Fe_{ox1} measured in the coretop sediment to the corresponding overlying water SPM for each site, assuming the two materials are the same, gives an Fe_{ox1} in the suspended particles of 214 - 301 nmol L^{-1} for MC, 43.0 - 287 nmol L^{-1} for BB, and 87.7 - 120 nmol L^{-1} for SC.

4.6 Iron behaviour during incubation experiments

The control carboy [dFe] was 5.6 – 5.9 nM across the three site experiments. Initial conditions prior to sediment addition in treated carboys (T0) were 5.0 ± 0.8 nM, 3.2 ± 1.1 nM, and 5.5 ± 0.3 nM for Sheldon Cove, Börgen Bay, and Marian Cove, which is lower than, or within error of, the control T0 [dFe]. Despite collection methods not being trace metal clean, control concentrations were highly consistent and within the range of regional values at depth (Ardiningsih et al., 2021; Bown et al., 2018; Sherrell et al., 2018), and so are likely representative of a background control. Henceforth we refer to the difference in [dFe] from the control and the mean spiked carboy [dFe] at individual timesteps as ΔdFe, and the equivalent for cFe (ΔcFe) and sFe (ΔsFe).

Following sediment addition, [dFe] peaked at 1 h (T1) in all three WAP bays. Mean [dFe] at T1 were 74.6 ± 8.2 nM, 179.5 ± 12.9 nM and 88.7 ± 11.8 nM at Sheldon Cove, Börgen Bay, and Marian Cove, respectively (Figure 3, Figure 4). A rapid decrease in [dFe] following the initial T1 peak is observed at all bays, and [dFe] appeared to stabilise at all sites within the experiment duration. Notably, beyond T12, the mean and individual carboy [dFe] at each bay exceed the control [dFe]. At both Börgen Bay and Marian Cove, ΔdFe concentrations after 48 h are +11 nM and +12 nM, respectively. At Sheldon Cove, the ΔdFe for T48 was +3.8 nM, with a mean [dFe] of 8.6 nM. For Marian Cove and Börgen Bay, the decay behaviour and endpoint ΔdFe suggest that ΔdFe will remain positive well beyond the elapsed experiment time.

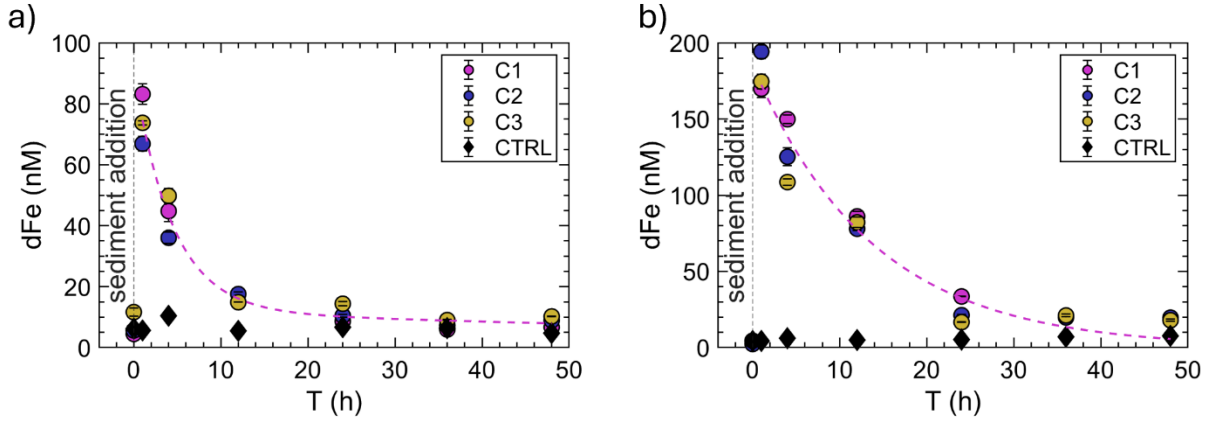

Figure 3: Evolution of [dFe] over time for sediment-water incubation experiments carried out at the West Antarctic Peninsula, for sediment and bottom waters collected from a) Sheldon Cove and b) Börgen Bay. Coloured dots represent the triplicate spiked carboys. Black diamonds are the control carboy [dFe], and the pink dotted lines represent the fitted exponential curves for the spiked carboys from T = 1. Error bars are plotted as ± 1 s.d.

At Marian Cove (WAP) sFe was also measured, facilitating the calculation of cFe as shown in Figure 4. The T0 [sFe] pre-sediment addition was 5.85 ± 0.38 nM, and the control T0 [sFe] was 6.54 ± 0.15 nM, whilst the control [cFe] was ~0.2 nM. Soluble Fe concentrations peaked at T1 with a ΔsFe of +17.3 ± 4.2 nM and proceeded to decline rapidly with time. For T36 and T48, the ΔsFe was < 1 nM. Therefore, the majority of ΔdFe during the experiment was represented by the colloidal phase. At T0, cFe/dFe was 0, rising to 73% at T1, with a ΔcFe of 65.5 ± 12.3 nM following sediment addition (Figure 4). The cFe/dFe

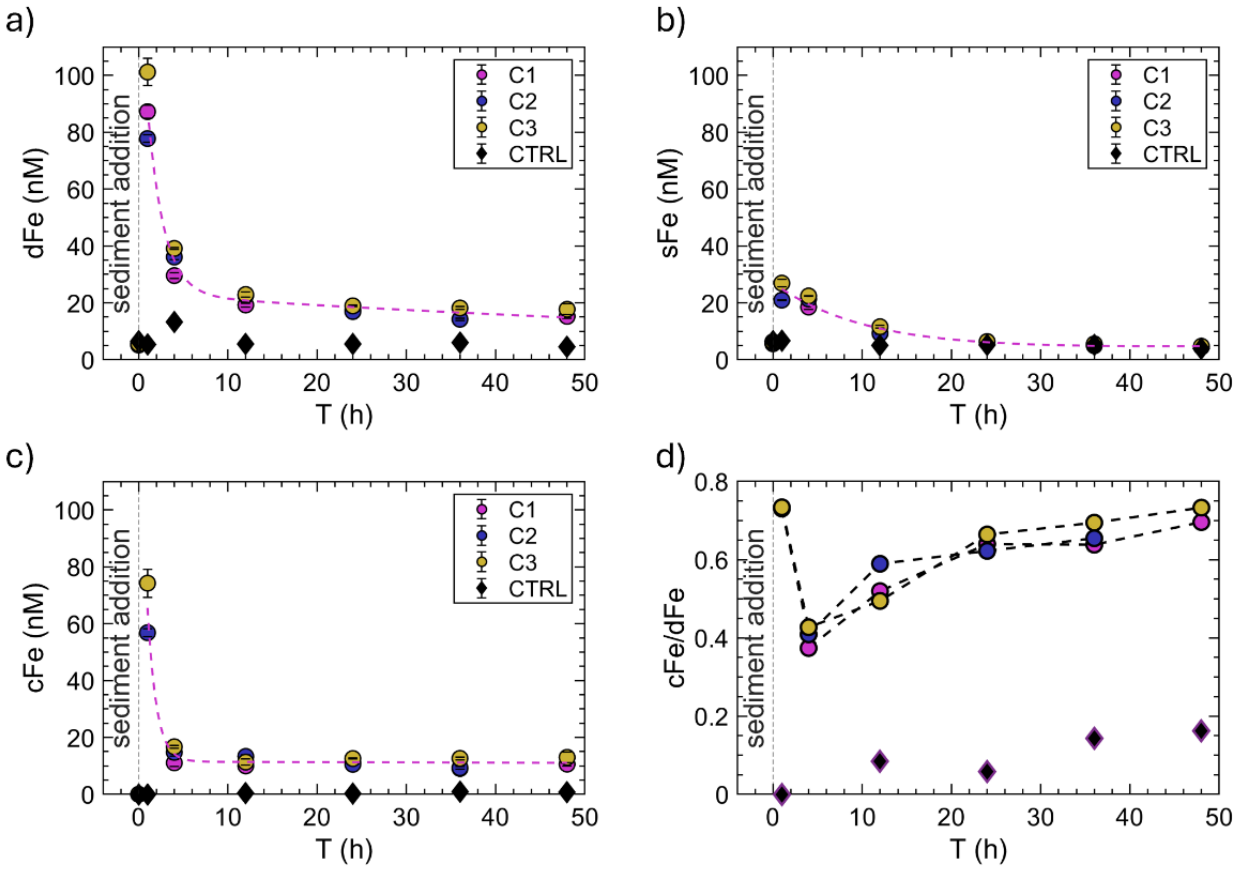

Figure 4: Sediment-water incubation results from Marian Cove for a) measured [dFe] b) measured [sFe], c) measured [cFe], and d) the ratio of cFe to dFe in individual replicates from T = 1. Coloured dots represent the sediment-added carboys in triplicate. Black diamonds represent the control experiment. The dotted lines in a), b), and c) represent the fitted exponential curve for spiked carboy concentrations, from T = 1.

was lowest at T4 following sediment addition (41%) but rose to 72% with an endpoint [cFe] of 11.0 ± 1.7 nM. The cFe/dFe at Marian Cove did not exhibit large variability between replicates (< 0.05 s.d.).

The ΔdFe (and ΔsFe, ΔcFe for Marian Cove) appeared to decrease exponentially with time. Exponential curves fitted to each dFe dataset had an r^2 of > 0.95. The terms for these fits are provided in the Supplementary Material and are plotted on the corresponding Figure 3 and Figure 4.

Prior to sediment addition and in control incubations, total dissolvable Fe (TdFe) and Mn (TdMn) were below instrument detection limit. Following sediment addition, T1 TdFe concentrations were > 60 µM, and taking the average of all replicate timesteps for each station, TdFe was 62 ± 17 µM, 94 ± 37 µM, and 101 ± 23 µM for Sheldon Cove, Börgen Bay, and Marian Cove, respectively (Figure 5). Iron and manganese behaviour with time for each site is summarised in Table 3.

During experiments, dFe can be lost from solution due to adsorption onto the bottle walls, which was not investigated. Solubility studies indicate that up to 20 – 30 % of dFe can be lost to adsorption onto bottle walls for high concentration samples (i.e. dFe > 1 nM) (Schlosser et al., 2011), which could bias our results by underestimating the released dFe. To mimic the process of sediment resuspension we shook the carboys prior to sampling which could result in an overestimation of dFe release over the experiment. Some gentle shaking will also have been experienced by ship movement. This approach was determined as more representative of the natural system than not shaking the carboys, which would leave sediment to settle and separate from the overlying water column. Due to the required volume to extract 180 mL sample plus rinsing volume at each timepoint, the volume of carboy setup (20 L) was required, and provision of a shaker of the required size to agitate sediment constantly was not possible, but this is recognised as a limitation of the experiment.

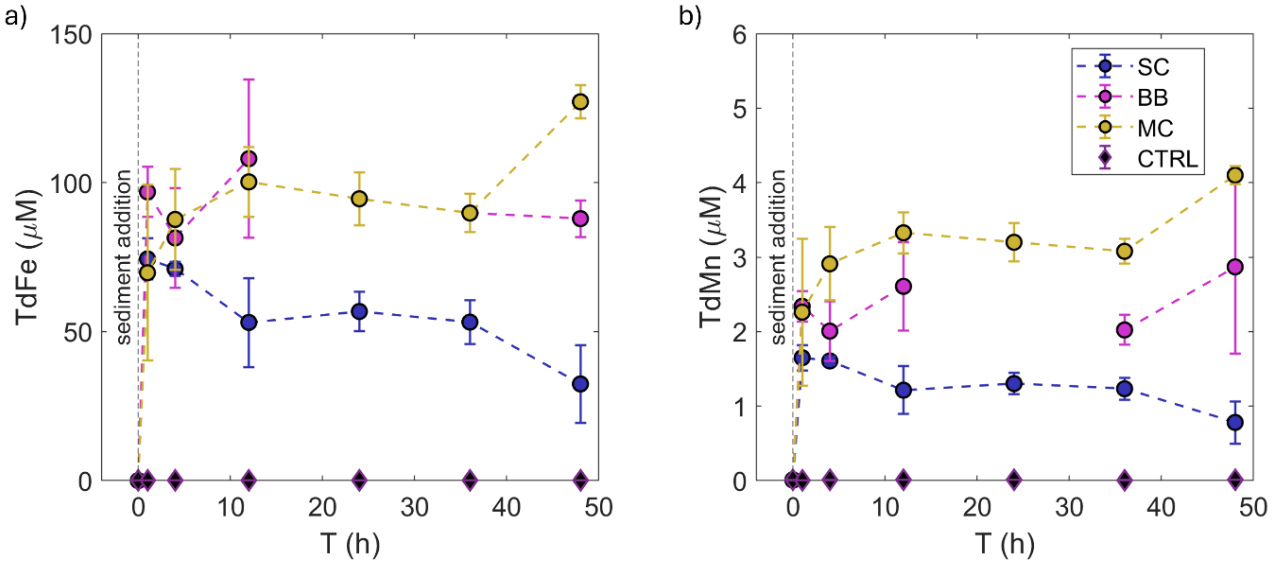

Figure 5: a) Total dissolvable iron concentrations and b) total dissolvable manganese concentrations for Sheldon Cove (SC), Börgen Bay (BB), and Marian Cove (MC) during sediment incubation experiments.

Table 3: Summary of sediment incubation experiment results for dissolved Fe phases at the WAP.

Station	Max ΔdFe	T48 ΔdFe	Max ΔcFe	T48 ΔcFe	Ctrl T48 cFe/dFe	T48 cFe/dFe
Unit	*nM*	*nM*	*nM*	*nM*	-	
Sheldon Cove	69.0 ± 8.2	3.8 ± 1.8	-	-	-	
Börgen Bay	175 ± 12.9	11.0 ± 0.9	-	-	-	
Marian Cove	83.3 ± 11.8	11.9 ± 1.8	65.5 ± 12.3	11.0 ± 1.7	0.16	0.72 ± 0.03

4.7 Velocity profiles/EK80 acoustic data at the West Antarctic Peninsula

The EK80 acoustic backscatter transects, and current velocity/direction data are shown in Figure 7 and Supplementary Figure S3 and S4. The dark shading of intense backscatter at the bottom of the EK80 profiles represents the bay bathymetry. Coherent aggregation of volume backscattering strength (Sv) exceeding -80 dB re 1 m^{-1} in the surface mixed layer is attributed to biology, such as krill swarms. Elevated backscatter near to bathymetric changes is interpreted as sediment plumes generated by seabed resuspension, forming plume-like structures that originate at bathymetric highs and extend laterally, rapidly detaching from the seabed and exhibiting limited vertical extent with diffuse, filamentous morphology, distinct from the more compact and internally coherent structure of biological aggregations. In Börgen Bay and Marian Cove particularly, this is evident as significantly increased backscatter proximal to bathymetric highs, with turbulence and particle mixing forming a plume-like structures that are most prominent down-current, in the lee of these bathymetric sills. At Sheldon Cove (Figure S4), backscatter is more homogeneous and intense throughout the water column. At the time of sampling, hydrographic measurements revealed presence of a glacial plume at Sheldon Cove, originating from Sheldon Glacier, and significant influence of particles was observed from proximal to the glacier edge and near the main bay sill (Jones et al. 2023). Radium-224 and thorium-228, tracers of sediment-derived solute and particle influence respectively, are highly enriched at depth in Sheldon Cove (Jones et al. 2023), so we infer that the particle load is elevated from both benthic exchange and a sediment-laden glacial plume, making any sediment resuspension indistinguishable from other processes.

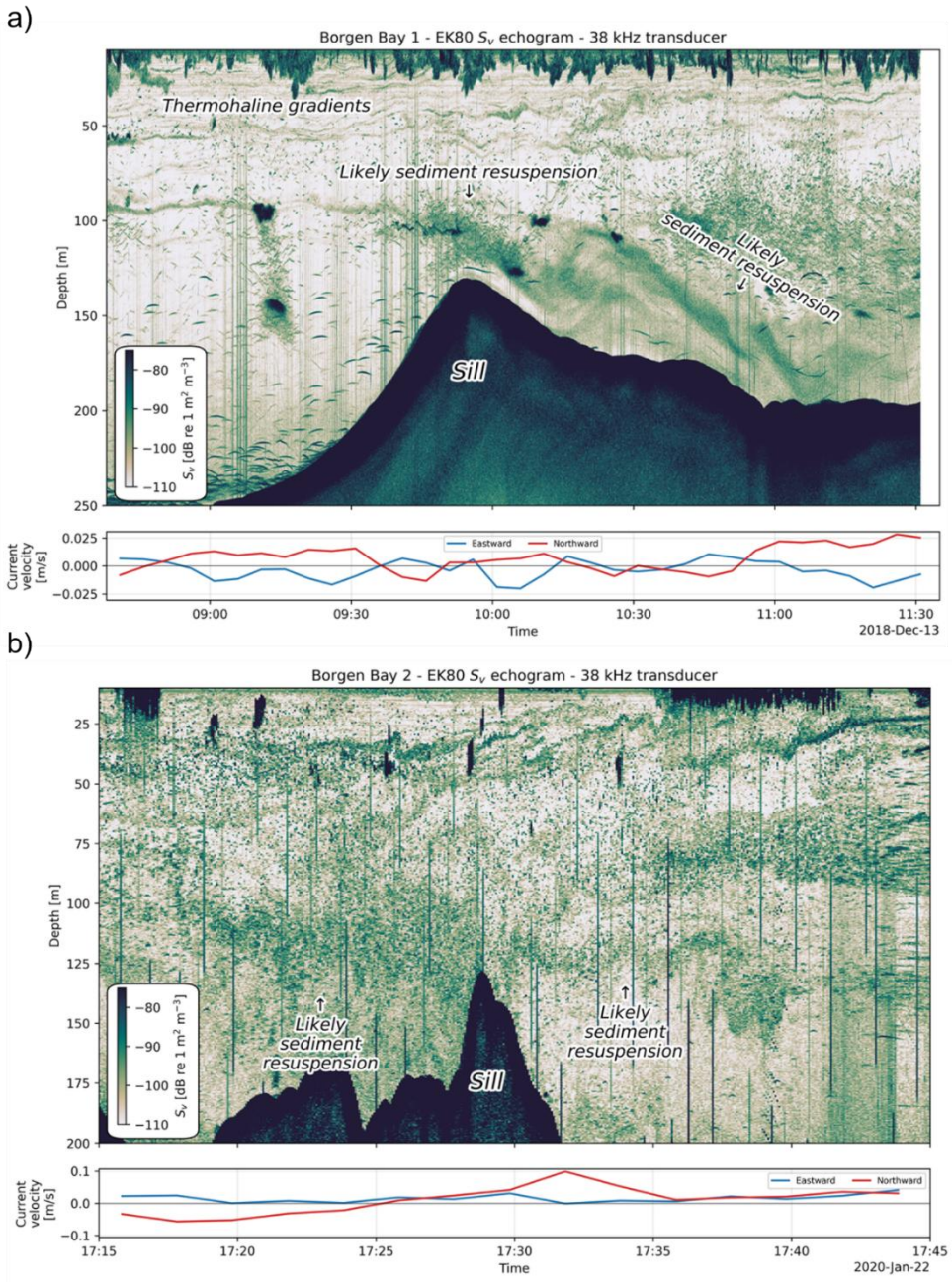

Figure 7: EK80 backscatter within the water column collecting in January 2020 from Marian Cove, showing a) the transect moving northeast into the bay; b) the transect moving southwest out of the bay. Lower panel shows current velocity averaged over depth. Backscatter from the seafloor is shown by backscatter values >-80 dB at the bottom of the images. High backscatter at shallower depths likely resembles krill swarms or other large biomass. See map figure S2 for track location.

5. Discussion

5.1 High supply of dissolved iron to bottom waters

Sediment addition in all mesocosms produced a sustained increase in bottom-water [dFe] of +4 to +12 nM relative to background. At Marian Cove, where cFe and sFe were measured, the initial Fe release appears to be both cFe and sFe (e.g. cFe/dFe of 0.4 at T4), and some sFe addition is retained over 12 – 24 h. The sustained dFe release was dominated by the colloidal phase, yielding a final [cFe] of 11 nM and a cFe/dFe ratio of 0.72—higher than the ocean-interior range of 0.4–0.6 (Kunde et al., 2019). Across WAP experiments, control [dFe] values were in the range of inner-shelf bottom water [dFe] of 4 – 33 nM, as measured near to Sheldon Cove, Adelaide Island, and Börgen Bay, Anvers Island (Ardiningsih et al., 2021; Bown et al., 2018; Sherrell et al., 2018). Therefore, despite the absence of trace-metal-clean sampling, contamination of background and T0 samples is likely minimal relative to total dFe.

The sustained ΔdFe of +4 to +12 nM indicates that coastal sediments mixed up into the water column can provide a significant source of stable dFe (sFe and cFe) to WAP bottom waters, exceeding typical Southern Ocean dFe of < 0.1 nM (Von der Heyden, 2014) by up to two orders of magnitude. In the context of shelf sediment resuspension, these results clearly indicate that short-term release of Fe from coastal shelf sediments is both sFe (i.e. largely bioavailable) and cFe, and that some component of the cFe remains stable in bottom waters on a timescale of days. Once in the water column, dFe can be stabilised by organic Fe-binding ligands on similar timescales, as observed in the Bransfield Strait (Buck et al., 2010) and Bellingshausen Sea (Ardiningsih et al., 2021). The data presented in Jones et al. (2025) supports this hypothesis for the WAP regions presented in this study, where DOC exceeded background levels, and organic C was aggregated with (nano)particulate Fe in the surface waters of Marian Cove, Sheldon Cove, and Börgen Bay.

The very high TdFe release (30–120 μM) during experiments and the high Fe_{ox1} measured in the sediment solid phase demonstrates a large reactive Fe pool delivered from sediments, and is in agreement with other studies demonstrating a highly labile component within Antarctic shelf bottom water particulate Fe, derived from under the ice sheet (Chinni et al., 2026). While rapid adsorption/desorption of reactive particulate Fe is well documented in hydrothermal plumes (Fitzsimmons et al., 2017), shelf studies typically emphasise scavenging and loss of dFe (Homoky et al., 2012), rather than the potential to provide a sustained source of dFe through desorption and dissolution. Our results highlight the need to consider particulate–colloidal exchange as a source of Fe, alongside scavenging and sinking, when evaluating shelf bioavailable Fe fluxes.

5.2 Sources of dissolved Fe

For Marian Cove and Sheldon Cove, the pore water dFe required to explain maximum incubation [dFe]—75 μM and 71 μM—far exceeds measured values of 2.7 μM and 1.1 μM. At Börgen Bay, dFe of ~170 μM would be required, assuming similar porosity, yet nearby pore water measurements show only 1.2 μM at 0.5 cm depth (Friberg et al., 2026), with oxic pore waters

to 3 cm and porosity of 0.744. Thus, measured pore water dFe at 0.25 cm accounts for <4% of the maximum released dFe, and only 25% and 27% of the sustained (T48) increase at Marian Cove and Sheldon Cove. Pore water dFe shows enrichment below 0.5 cm (8.27 and 2.23 μM at 0.75 and 1.25 cm in Sheldon Cove; 21 and 24 μM in Marian Cove) but remains insufficient to explain incubation increases (Figure 6).

A significant component (73 - 75%) of the total sustained dFe release is therefore not accounted for by pore water measurements. Typically, enriched dissolved Fe concentrations in pore waters are indicative of reducing (i.e. anoxic) conditions, where microbial activity uses Fe(III) as an electron acceptor, and generates reduced and soluble Fe(II). Oxygen at all sites in the top 3 cm of sediments exceeds anoxic levels (< 15 – 20 μM). At Sheldon Cove, O_2 reaches a minimum of 32 μM in the top 3 cm, the lowest recorded from all sites. Nitrate and nitrite profiles indicate that the coretop sediment (0 – 0.5 cm) lies above the redox boundary, defined here as the nitrate penetration depth (Burdige & Christensen, 2022). The measurable pore water dFe above this boundary suggests dynamic redox conditions, abundant reactive Fe (oxyhydr)oxides, and a mechanism of that supplies dissolved Fe to the oxic sediment that could either be rapid upward transport of reduced iron from the shallow more typically ferruginous zone below, such as observed in fjord settings (Ebner et al., 2026), or the non-reductive dissolution of Fe i.e. a flux of desorption or chemical dissolution that is generally thought to supply Fe to the colloidal phase (Radic et al., 2011).

Dissolved Fe release from sediment solids occurs through several geochemical and physico-chemical pathways. Reductive dissolution of Fe (oxyhydr)oxides, magnetite, and Fe(III) in clays produces soluble Fe(II) in reducing sediments, resulting in pore waters enriched in Fe (Dong et al., 2009), with concentrations generally increasing with depth. This reductive mobilisation is a key component of sedimentary redox cycling globally (Raiswell & Canfield, 2012). Diffusion, bioturbation, bioirrigation, or resuspension can transport Fe-rich pore waters into the overlying water column, supplying dFe to the ocean (Dale et al., 2015). Reductive dissolution rates depend on Fe mineral reactivity and environmental conditions, and for less reactive phases occur over days to years (Poulton et al., 2004; Raiswell & Canfield, 2012).

The steep increase in pore water dFe over the top 1 cm and elevated dFe relative to typical shelf dFe pore water profiles from the region (e.g.Burdige & Christensen, 2022), are indicative of upwards diffusive fluxes of reduced Fe(II), with subsequent oxidation of reduced Fe to form Fe(III)-rich precipitates in surface sediments. With respect to the incubation experiments, the highest sustained supply of dFe to bottom waters was observed in Marian Cove, where pore water O_2 was highest, indicating a decoupling of dFe concentrations and oxygen concentrations. Our observations suggest that resuspension of sediments in glacier-proximal settings is a key source of dFe to overlying waters, as reactive Fe in oxic sediments is remobilised and released. Therefore, this could point towards the important role that non-reductive dissolution plays in supplying colloidal Fe (and soluble Fe) from the lithogenic, solid phase of the sediments, in these environments, as observed elsewhere in oxic deep-sea and margin sediments (Conway & John, 2014; Homoky et al., 2021; Homoky et al., 2013).

The rapid (< 1 hr) release of dFe, predominantly in the colloidal phase (e.g. Figure 4c, d), following sediment addition at the three WAP stations is suggestive of a highly reactive Fe pool in glaciomarine WAP sediments that is mobilised when mixed with bottom waters, either from colloids loosely bound to mineral surfaces, released dFe by the physical process of mixing, or

dFe present within the pores between sediments that was not captured by pore water extraction. At Marian Cove, some sFe is retained over the first 24h of the experiment, indicating a truly bioavailable source of Fe is supplied and not immediately lost from sediments, but that this is not retained within the seawater beyond ~24 – 36 h. Within 48 h, 85–95% of the released dFe (driven by cFe) is lost, likely through adsorption onto particles or aggregation and precipitation.

5.3 The solid-sediment iron composition

The WAP sediments proximal to the glacier termini are lithogenic in origin, as determined by SEM-EDS, deriving primarily from the physical weathering of bedrock on the peninsula (Pereira et al., 2018). Sediments mostly consist of an Al-Si rich mineral phase, with a composition comparable to the average wt% of common elements in the upper crust (Figure S1; Angino 1996), indicative of production and transportation of physically eroded silicate bedrock, and Fe-rich phases. Using the same sequential extraction techniques, Burdige and Christensen (2022) found that Fe oxides (Fe_{ox1} + Fe_{ox2}) accounted for 29% and 19% of the total Fe at 0 – 2 cm depth for inshore and offshore WAP shelf sediments, respectively. The remaining sediment consisted of more refractory silicate minerals, with total sulfidic Fe(II) and unsulfidized Fe(II) produced by reductive dissolution <1 % of total Fe. Operationally defined highly reactive Fe_{ox1} phases comprised 3.0 – 6.1%, highest for inshore sediments. In this study, we find an (Fe_{ox1} + Fe_{ox2}) component of 7.5 – 31.3 % of total Fe, and an Fe_{ox1} component of 5.3 – 17.7 % (Table 4). Notably, the operationally defined most reactive Fe fraction (Fe_{ox1}) is highest in inshore and glacial sediments, with Marian Cove, King George Island exhibiting the highest most reactive Fe component in both this study and in Burdige and Christensen (2022).

Poorly crystalline amorphous phase Fe (oxyhydr)oxides such as ferrihydrite and lepidocrocite, targeted in the Fe_{ox1} leach, are among the most reactive Fe minerals and readily undergo dissolution or surface-layer desorption. These phases constitute 5.3 – 17.7 % of the total Fe in the collected surface sediments and may contribute to the colloidal Fe phase. The dFe flux from oxic sediments remains sparsely measured (Homoky et al., 2016), poorly represented in ocean biogeochemical models (Tagliabue et al., 2016), and rarely included in benthic Fe mobilisation flux estimates and calculations (Burdige & Christensen, 2022).

Multiple studies of glaciated bays and fjords in Greenland and the Antarctic show that glacial physical erosion of bedrock and export of reactive glacial flour enriches regional sediments in reactive forms of Fe (and Mn) (Hawkings et al., 2017; Meire et al., 2017). Our results show that glacier-proximal surface sediments contain a highly reactive solid-phase Fe pool, evidenced by the release of 30–90 μM TdFe and a readily dissolvable or desorptive cFe flux during incubations. This highlights a previously underrepresented cFe flux during sediment resuspension that remains stable over short timescales (days). Although long-term stability was not measured here, Cheize et al. (2019) observed persistent dissolved Fe (and Mn) release from basaltic particles over 14 months. We also emphasise the need to assess the reactivity and desorption potential

485 of Fe in >0.2 µm phases, including exchange between >0.2 µm and >0.02 µm fractions, and to investigate the often overlooked 0.2–0.45 µm colloidal fraction as a potentially important reservoir of dFe.

Table 4: Comparison of the total Fe and Fe oxide composition at the three WAP glacial sites, compared with the broader WAP shelf.

490

Station	Fe_T	$Fe_{ox1} + Fe_{ox2}$: Fe_T	Fe_{ox1}:Fe_T	TDFe:Fe_T
	Wt%	%	%	%
Sheldon Cove	4.0 ± 1.0	7.5 ± 2.0	5.3 ± 1.0	6.1 ± 0.3
Börgen Bay	5.2 ± 0.2	14.7 ± 2.0	9.7 ± 1.0	8.5 ± 0.5
Marian Cove	5.4 ± 1.0	31 ± 0.7	17.7 ± 0.4	10.4 ±1.1
Inshore*	4.7 ± 0.3	29 ± 1	6.1	
Offshore*	4.8 ± 1.3	19 ± 3	3.0	

*As reported in the 0 – 2 cm sediment layer in sediments from the West Antarctic Peninsula shelf, by Burdige & Christensen (2022). The inshore and offshore stations in that study are in Supplementary Figure S5.

4.4 Resuspension events as a key source of Fe to WAP bays

The dFe of Circumpolar Deep Water (CDW) is relatively high (~ 0.5 nM), yet Antarctic shelf waters often exceed this at depth in the Amundsen Sea (Gerringa et al., 2012), Ross Sea (Gerringa et al., 2015), and near the coast in Marguerite Trough and Marguerite Bay (Sherrell et al., 2018). Sediment studies further indicate dFe in pore waters is elevated in fjord sites relative to
495 the coast (Burdige & Christensen, 2022; Henkel et al., 2018; Monien et al., 2014).

In glacier-proximal settings, deepwater overflow and glacial meltwater drive strong vertical and lateral mixing and benthic exchange, as observed at Sheldon Cove (Cape et al., 2019; Jones et al., 2023; Venables et al., 2017). EK80 data from Marian Cove and Börgen Bay, indicate frequent suspension of material (Supplementary Figures S2 – S4), and VMADCP-derived current velocities, presented averaged over depth, show rapidly changing flow directions, implying regular resuspension is
500 possible. Likely drivers of resuspension include tidal and wind driven circulation, calving-induced tsunamis (Meredith et al.,

2022), and subsequent interaction with bathymetric features. Venables et al. (2017) use glider conductivity, temperature, depth, and turbidity data to demonstrate enhanced mixing and turbulence over bathymetric highs. Together, these nearshore processes provide multiple pathways for resuspension of sediment rich in both reactive dFe and cFe.

Using the sustained release of dFe observed in each incubation (3.8 – 11.8 nM) and the Fe_{ox1} content of added sediments, we estimate the potential resuspension flux of dFe and Fe_{ox1} from WAP glaciomarine sediments. Implementing a conservative sediment resuspension depth of 0.1 cm (Burdige and Komada, 2020), each resuspension event would release 2.5 – 7.9 μmol m^{-2} of dFe and 36 – 110 mmol m^{-2} of Fe_{ox1}.

The impact of the glaciomarine sedimentary Fe pool upon the sustained supply of Fe to the WAP shelf water column depends upon the frequency of resuspension events. Burdige and Christensen (2022) assume one sediment resuspension event per year. Our ADCP and backscatter suggest that in near-coastal regions, circulation processes and their interaction with bathymetry drive sediment mixing into the water column on a daily to weekly frequency during ice free periods, driven by winds, tidal processes, or turbulent overflows. If we assume sediment is resuspended between once per day and once per week over six months (i.e. 26 – 182 times per year) and take the range of sustained dFe addition from sediment in the incubation experiments at each site, the flux of dFe to the water column from physical resuspension would be 0.18 – 1.3 μmol m^{-2} d^{-1} at SC, 0.52 – 3.7 μmol m^{-2} d^{-1} at BB, and 0.56 – 4.0 μmol m^{-2} d^{-1} at MC. These values are within the expected range of benthic dFe fluxes to oxic bottom waters (i.e. $O_2 > 63$ μM) reported by Dale et al. (2015). The approach in Dale et al. (2015) accounts for molecular diffusion, bioturbation, bio-irrigation, and surface sediment physico-chemical processes, and does not account for fluxes of Fe by sediment resuspension. Notably, our estimates of dFe released from oxic sediments by sediment resuspension are lower yet comparable with estimates of total mixed-layer Fe supply from the continental margin of 7.6 ± 5.0 μmol m^{-2} d^{-1} in de Jong et al. (2015). Our results suggest that physical resuspension of reactive oxic sediments could be an important and underrepresented source of water column dFe to the Antarctic shelf, particularly at the coast. Conservatively assuming each WAP glacier (n = 674; Cook et al. 2016) has a 5 km^2 fjord or embayment and experiences the drivers of sediment resuspension are common across the WAP coast, this gives a total area of 3370 km^2, or a physical resuspension dFe flux of 610 – 13,000 mol yr^{-1}.

Further work to understand the frequency of Antarctic shelf oxic sediment resuspension year-round, and the scale of export of this dFe source, would help determine the impact of sediment resuspension upon potentially Fe-limited regions such as the broader Southern Ocean. Understanding how sedimentary reactive and dissolved Fe is transported into the water column, and how bioavailable it is, is essential for assessing its influence on surface-ocean Fe supply to primary producers. Although the bioavailability of fresh, glaciomarine sediment Fe from the WAP has not yet been directly measured, there is increasing evidence that (sub-)Antarctic glacier-derived Fe is more bioavailable than other sources (Fourquez et al., 2023; Shoenfelt et al., 2017; Stimpfle et al., 2026; Wyatt et al., 2023). The WAP shelf is characterised by off-shelf export via deep water masses (Moffat and Meredith, 2018), and recent work shows that glacially and sediment-derived Fe can be transported from the Antarctic shelf to the central Weddell Sea (Tian et al., 2026). Regions with short transport pathways between fresh glaciogenic

sediments and Fe-limited waters—such as the northern WAP—may therefore be especially important for supplying potentially bioavailable Fe to the Southern Ocean mixed layer (Monien et al., 2017). Marian Cove, King George Island, sits close to the Bransfield Strait, where rapid circulation from the Bransfield Current transports water to the potentially Fe-limited Scotia Sea (Dulaiova et al., 2009; Hatta et al., 2013). The Marian Cove incubation showed the highest endpoint increase in dFe, with 73% of this in the colloidal phase, and the highest sediment Fe_{ox1} (9 mg g^{-1}) and TdFe (~100 μM), indicating active solid–dissolved phase exchange and a substantial supply of bioavailable dFe to the water column. Glacial fjords and embayments in the northern WAP may therefore play a disproportionately important role in supplying Fe to the Southern Ocean mixed layer relative to other Fe sources—an influence that has so far been largely overlooked.

6 Conclusions

This study provides strong evidence that resuspension of recently deposited glaciomarine sediments supply an important flux of both dissolved and reactive Fe to the oxic bottom waters of the Antarctic shelf. Driven by Fe supply to the colloidal phase, sediments incubated from the northern WAP glacial fjord provided the highest sustained increase in dissolved Fe following sediment resuspension, and export potential to the Southern Ocean mixed layer, where Fe limitation is most prevalent. Further investigation of the transport of reactive Fe from sediments to the broader WAP shelf would enable evaluation of the spatial significance of these findings and help constrain the total suspended sediment flux of reactive Fe attributed to glacial fjords. as glaciers continue to melt and retreat (Cook et al. 2016), and seasonal sea ice extent and duration changes (Ducklow et al., 2013), it will be critical to further understand the role of tides, wind, and fjord circulation processes upon the frequency of sediment resuspension across the WAP. In turn, understanding how these processes influence the resuspension and transport of sediment-derived Fe will be essential for predicting future Fe availability and ecosystem functioning across the Antarctic shelf and Southern Ocean.

Data availability statement:

Solid sediment SEM-EDS, sediment extraction, and incubation data is available in the Supplementary Dataset. Pore water iron, nitrate, and oxygen data is available from the Polar Data Centre: Friberg et al. (2026).

ICEBERGS 2 (JR18003) and ICEBERGS 3 (JR19002) cruise CTD data is publicly available from the UK BODC repository: Scourse et al. (2022).

Multibeam bathymetry data is available from (Retallick et al., 2021).

Acknowledgements

We also thank the officers, crew, and scientists abroad the JR19002 and JR18003 cruises for all assistance and support.

Financial support

The authors acknowledge funding from Radium in Changing Environments: A Novel Tracer of Iron Fluxes at Ocean Margins (RaCE:TraX) grant (NE/P017630/1) (A.L.A.) and the National Environmental Research Council INSPIRE Doctoral Training Partnership (NE/S0072101) (R.L.J.). The OCTONAUTS CASS BAS grant supported the EK80 data collection on the ICEBERGS cruises (PI – K.S.).

Supplementary Material

The following file contains the supplementary Data to this article:
Supplementary Data 1.
The following contains supplementary Figures and Tables to this article:
Supplementary Material

Author contributions

Writing – original draft: R.L.J.. Writing – review and editing: all coauthors. Conceptualization: R.L.J, A.L.A., M.C.L.. Investigation: R.L.J, M.C.L., L.F., T. E., G.D., B.L., K.S., K.V.L., K.R., and A.L.A.. Project administration and funding acquisition: J.S., A.L.A., K.S.. Visualization: R.L.J and T.E..

Competing interests

The authors declare that they have no competing interests.

Disclaimer

Copernicus Publications remains neutral with regard to jurisdictional claims made in the text, published maps, institutional affiliations, or any other geographical representation in this paper. While Copernicus Publications makes every effort to include appropriate place names, the final responsibility lies with the authors. Views expressed in the text are those of the authors and do not necessarily reflect the views of the publisher.

References

Annett, A. L., Fitzsimmons, J. N., Séguret, M. J., Lagerström, M., Meredith, M. P., Schofield, O., & Sherrell, R. M. (2017). Controls on dissolved and particulate iron distributions in surface waters of the Western Antarctic Peninsula shelf. *Marine Chemistry*, *196*, 81-97.

Ardelan, M., Holm-Hansen, O., Hewes, C., Reiss, C. S., Silva, N., Dulaiova, H., Steinnes, E., & Sakshaug, E. (2010). Natural iron enrichment around the Antarctic Peninsula in the Southern Ocean. *Biogeosciences*, *7*(1), 11-25.

Ardiningsih, I., Seyitmuhammedov, K., Sander, S. G., Stirling, C. H., Reichart, G.-J., Arrigo, K. R., Gerringa, L. J., & Middag, R. (2021). Fe-binding organic ligands in coastal and frontal regions of the western Antarctic Peninsula. *Biogeosciences*, *18*(15), 4587-4601.

Bowie, A., & Lohan, M. (2009). Determination of iron in seawater. In 'Practical Guidelines for the Analysis of Seawater'.(Ed. O. Wurl.) pp. 235–258. In: CRC Press, Taylor Francis group: London.

Bown, J., van Haren, H., Meredith, M. P., Venables, H. J., Laan, P., Brearley, J. A., & de Baar, H. J. (2018). Evidences of strong sources of DFe and DMn in Ryder Bay, Western Antarctic Peninsula. *Philosophical Transactions of the Royal Society A: Mathematical, Physical and Engineering Sciences*, *376*(2122), 20170172.

Browning, T. J., & Moore, C. M. (2023). Global analysis of ocean phytoplankton nutrient limitation reveals high prevalence of co-limitation. *Nature communications*, *14*(1), 5014.

Buck, K. N., Selph, K. E., & Barbeau, K. A. (2010). Iron-binding ligand production and copper speciation in an incubation experiment of Antarctic Peninsula shelf waters from the Bransfield Strait, Southern Ocean. *Marine Chemistry*, *122*(1-4), 148-159.

Burdige, D. J., & Christensen, J. P. (2022). Iron biogeochemistry in sediments on the western continental shelf of the Antarctic Peninsula. *Geochimica et Cosmochimica Acta*, *326*, 288-312.

Cape, M. R., Straneo, F., Beaird, N., Bundy, R. M., & Charette, M. A. (2019). Nutrient release to oceans from buoyancy-driven upwelling at Greenland tidewater glaciers. *Nature Geoscience*, *12*(1), 34-39.

Cheize, M., Planquette, H. F., Fitzsimmons, J. N., Pelleter, E., Sherrell, R. M., Lambert, C., Bucciarelli, E., Sarthou, G., Le Goff, M., Liorzou, C., Chéron, S., Viollier, E., & Gayet, N. (2019). Contribution of resuspended sedimentary particles to dissolved iron and manganese in the ocean: An experimental study. *Chemical Geology*, *511*, 389-415. https://doi.org/10.1016/j.chemgeo.2018.10.003

Chinni, V., Steffen, J. M., Stammerjohn, S. E., St-Laurent, P., Herbert, L. C., Yager, P. L., Conway, T. M., Fitzsimmons, J. N., & Sherrell, R. M. (2026). Iron supply to the Amundsen Sea, Antarctica is dominated by circumpolar deepwater and continental subglacial sources. *Communications Earth & Environment*, *7*(1), 162.

Conway, T. M., & John, S. G. (2014). Quantification of dissolved iron sources to the North Atlantic Ocean. *Nature*, *511*(7508), 212.

Cook, A. J., Holland, P., Meredith, M., Murray, T., Luckman, A., & Vaughan, D. G. (2016). Ocean forcing of glacier retreat in the western Antarctic Peninsula. *Science*, *353*(6296), 283-286.

De Jong, J., Schoemann, V., Lannuzel, D., Croot, P., de Baar, H., & Tison, J. L. (2012). Natural iron fertilization of the Atlantic sector of the Southern Ocean by continental shelf sources of the Antarctic Peninsula. *Journal of Geophysical Research: Biogeosciences*, *117*(G1).

De Jong, J., Stammerjohn, S., Ackley, S., Tison, J.-L., Mattielli, N., & Schoemann, V. (2015). Sources and fluxes of dissolved iron in the Bellingshausen Sea (West Antarctica): The importance of sea ice, icebergs and the continental margin. *Marine Chemistry*, *177*, 518-535.

De Jonge, V., & Van Beuselom, J. (1992). Contribution of resuspended microphytobenthos to total phytoplankton in the Ems estuary and its possible role for grazers. *Netherlands Journal of Sea Research*, *30*, 91-105.

De Robertis, A., & Higginbottom, I. (2007). A post-processing technique to estimate the signal-to-noise ratio and remove echosounder background noise. *ICES Journal of Marine Science*, *64*(6), 1282-1291.

Demer, D. A., Berger, L., Bernasconi, M., Bethke, E., Boswell, K., Chu, D., Domokos, R., Dunford, A., Fässler, S., & Gauthier, S. (2015). *Calibration of acoustic instruments*. ICES Cooperative Research Reports (CRR).

Dold, B., Gonzalez-Toril, E., Aguilera, A., Lopez-Pamo, E., Cisternas, M., Bucchi, F., & Amils, R. (2013). Acid rock drainage and rock weathering in Antarctica: important sources for iron cycling in the Southern Ocean. *Environmental science & technology*, *47*(12), 6129-6136.

Domack, E. W., Foss, D. J., Syvitski, J. P., & McClennen, C. E. (1994). Transport of suspended particulate matter in an Antarctic fjord. *Marine Geology*, *121*(3-4), 161-170.

Ducklow, H. W., Fraser, W. R., Meredith, M. P., Stammerjohn, S. E., Doney, S. C., Martinson, D. G., Sailley, S. F., Schofield, O. M., Steinberg, D. K., & Venables, H. J. (2013). West Antarctic Peninsula: an ice-dependent coastal marine ecosystem in transition. *Oceanography*, *26*(3), 190-203.

Dulaiova, H., Ardelan, M. V., Henderson, P. B., & Charette, M. A. (2009). Shelf-derived iron inputs drive biological productivity in the southern Drake Passage. *Global Biogeochemical Cycles*, *23*(4).

Ebner, B., Henkel, S., Kraal, P., Müller, D., Köster, M., Staubwasser, M., Laufer-Meiser, K., Kattein, L., Geibert, W., & Kasten, S. (2026). Drivers of benthic iron fluxes and the Pore-water iron isotopic signature in surface sediments of South Georgia fjords, sub-Antarctica. *Global Biogeochemical Cycles*, *40*(4), e2025GB008856.

Elrod, V. A., Berelson, W. M., Coale, K. H., & Johnson, K. S. (2004). The flux of iron from continental shelf sediments: A missing source for global budgets. *Geophysical Research Letters*, *31*(12), n/a-n/a. https://doi.org/10.1029/2004gl020216

Fisher, B. J., Faust, J. C., Moore, O. W., Peacock, C. L., & März, C. (2021). Uncovering the influence of methodological variations on the extractability of iron-bound organic carbon. *Biogeosciences*, *18*(11), 3409-3419.

Fitzsimmons, J. N., John, S. G., Marsay, C. M., Hoffman, C. L., Nicholas, S. L., Toner, B. M., German, C. R., & Sherrell, R. M. (2017). Iron persistence in a distal hydrothermal plume supported by dissolved–particulate exchange. *Nature Geoscience*, *10*(3), 195.

Fourquez, M., Janssen, D. J., Conway, T. M., Cabanes, D., Ellwood, M. J., Sieber, M., Trimborn, S., & Hassler, C. (2023). Chasing iron bioavailability in the Southern Ocean: Insights from Phaeocystis antarctica and iron speciation. *Science Advances*, *9*(26), eadf9696.

Friberg, L., Annett, A. L., Sales de Freitas, F., Woodward, E. M. S., & Hendry, K. R. (2026). *Benthic silicon fluxes and sediment porewater chemistry in Sheldon Cove, Borgen Bay and Marian Cove, West Antarctic Peninsula, in January 2020 (Version 1.0)*. https://doi.org/https://doi.org/10.5285/f8f72bf5-035b-4851-8a21-d278485081b1

Gargett, A., Wells, J., Tejada-Martinez, A., & Grosch, C. (2004). Langmuir supercells: A mechanism for sediment resuspension and transport in shallow seas. *Science*, *306*(5703), 1925-1928.

Gerringa, L., Laan, P., Van Dijken, G., Van Haren, H., De Baar, H., Arrigo, K., & Alderkamp, A.-C. (2015). Sources of iron in the Ross Sea Polynya in early summer. *Marine Chemistry*, *177*, 447-459.

Gerringa, L. J., Alderkamp, A.-C., Laan, P., Thuroczy, C.-E., De Baar, H. J., Mills, M. M., van Dijken, G. L., van Haren, H., & Arrigo, K. R. (2012). Iron from melting glaciers fuels the phytoplankton blooms in Amundsen Sea (Southern Ocean): Iron biogeochemistry. *Deep Sea Research Part II: Topical Studies in Oceanography*, *71*, 16-31.

Hatta, M., Measures, C., Selph, K., Zhou, M., & Hiscock, W. (2013). Iron fluxes from the shelf regions near the South Shetland Islands in the Drake Passage during the austral-winter 2006. *Deep Sea Research Part II: Topical Studies in Oceanography*, *90*, 89-101.

Hawkings, J. R., Wadham, J. L., Benning, L. G., Hendry, K. R., Tranter, M., Tedstone, A., Nienow, P., & Raiswell, R. (2017). Ice sheets as a missing source of silica to the polar oceans. *Nature communications*, *8*(1), 1-10.

Hawkings, J. R., Wadham, J. L., Tranter, M., Raiswell, R., Benning, L. G., Statham, P. J., Tedstone, A., Nienow, P., Lee, K., & Telling, J. (2014). Ice sheets as a significant source of highly reactive nanoparticulate iron to the oceans. *Nature communications*, *5*(1), 1-8.

Henkel, S., Kasten, S., Hartmann, J. F., Silva-Busso, A., & Staubwasser, M. (2018). Iron cycling and stable Fe isotope fractionation in Antarctic shelf sediments, King George Island. *Geochimica et Cosmochimica Acta*, *237*, 320-338.

Hepburn, L. E., Butler, I. B., Boyce, A., & Schröder, C. (2020). The use of operationally-defined sequential Fe extraction methods for mineralogical applications: A cautionary tale from Mössbauer spectroscopy. *Chemical Geology*, *543*, 119584.

Homoky, W. B., Conway, T. M., John, S. G., König, D., Deng, F., Tagliabue, A., & Mills, R. A. (2021). Iron colloids dominate sedimentary supply to the ocean interior. *Proceedings of the National Academy of Sciences*, *118*(13), e2016078118.

Homoky, W. B., John, S. G., Conway, T. M., & Mills, R. A. (2013). Distinct iron isotopic signatures and supply from marine sediment dissolution. *Nature communications*, *4*(1), 2143. https://doi.org/10.1038/ncomms3143

Homoky, W. B., Weber, T., Berelson, W. M., Conway, T. M., Henderson, G. M., Van Hulten, M., Jeandel, C., Severmann, S., & Tagliabue, A. (2016). Quantifying trace element and isotope fluxes at the ocean–sediment boundary: a review. *Philosophical Transactions of the Royal Society A: Mathematical, Physical and Engineering Sciences*, *374*(2081), 20160246.

Jones, R. L., Hawkings, J. R., Meredith, M. P., Lohan, M. C., Moore, O. W., Sherrell, R. M., Fitzsimmons, J. N., Kazemian, M., Araki, T., & Kaulich, B. (2025). Antarctic glaciers export carbon-stabilised iron (II)-rich particles to the surface Southern Ocean. *Nature communications*, *16*(1), 5015.

Jones, R. L., Meredith, M. P., Lohan, M. C., Woodward, E. M. S., Van Landeghem, K., Retallick, K., Flanagan, O., Vora, M., & Annett, A. L. (2023). Continued glacial retreat linked to changing macronutrient supply along the West Antarctic Peninsula. *Marine Chemistry*, *251*, 104230.

Kunde, K., Wyatt, N. J., González-Santana, D., Tagliabue, A., Mahaffey, C., & Lohan, M. C. (2019). Iron Distribution in the Subtropical North Atlantic: The Pivotal Role of Colloidal Iron. *Global Biogeochemical Cycles*, *33*(12), 1532-1547. https://doi.org/10.1029/2019gb006326

Lam, P. J., Ohnemus, D. C., & Marcus, M. A. (2012). The speciation of marine particulate iron adjacent to active and passive continental margins. *Geochimica et Cosmochimica Acta*, *80*, 108-124. https://doi.org/10.1016/j.gca.2011.11.044

Laufer-Meiser, K., Michaud, A. B., Maisch, M., Byrne, J. M., Kappler, A., Patterson, M. O., Røy, H., & Jørgensen, B. B. (2021). Potentially bioavailable iron produced through benthic cycling in glaciated Arctic fjords of Svalbard. *Nature communications*, *12*(1), 1349.

Lee, W.-J., Setiawan, L., Tuguinay, C., Mayorga, E., & Staneva, V. (2024). Interoperable and scalable echosounder data processing with Echopype. *ICES Journal of Marine Science*, *81*(10), 1941-1951.

Leventer, A., & Dunbar, R. (1985). Suspended particulate matter in Antarctic coastal waters. *Antarc. JUS*, *20*(5), 100-103.

Liu, X., & Millero, F. J. (2002). The solubility of iron in seawater. *Marine Chemistry*, *77*(1), 43-54.

Martin, J. H. (1990). Glacial-interglacial CO2 change: The iron hypothesis. *Paleoceanography*, *5*(1), 1-13.

Meire, L., Mortensen, J., Meire, P., Juul-Pedersen, T., Sejr, M. K., Rysgaard, S., Nygaard, R., Huybrechts, P., & Meysman, F. J. (2017). Marine-terminating glaciers sustain high productivity in Greenland fjords. *Global Change Biology*, *23*(12), 5344-5357.

Meredith, M. P., Falk, U., Bers, A. V., Mackensen, A., Schloss, I. R., Ruiz Barlett, E., Jerosch, K., Silva Busso, A., & Abele, D. (2018). Anatomy of a glacial meltwater discharge event in an Antarctic cove. *Philosophical Transactions of the Royal Society A: Mathematical, Physical and Engineering Sciences*, *376*(2122), 20170163.

Meredith, M. P., Inall, M. E., Brearley, J. A., Ehmen, T., Sheen, K., Munday, D., Cook, A., Retallick, K., Van Landeghem, K., & Gerrish, L. (2022). Internal tsunamigenesis and ocean mixing driven by glacier calving in Antarctica. *Science Advances*, *8*(47), eadd0720.

Meredith, M. P., Stammerjohn, S. E., Venables, H. J., Ducklow, H. W., Martinson, D. G., Iannuzzi, R. A., Leng, M. J., Van Wessem, J. M., Reijmer, C. H., & Barrand, N. E. (2017). Changing distributions of sea ice melt and meteoric water west of the Antarctic Peninsula. *Deep Sea Research Part II: Topical Studies in Oceanography*, *139*, 40-57.

Meslard, F., Bourrin, F., Many, G., & Kerhervé, P. (2018). Suspended particle dynamics and fluxes in an Arctic fjord (Kongsfjorden, Svalbard). *Estuarine, Coastal and Shelf Science*, *204*, 212-224.

Monien, D., Monien, P., Brünjes, R., Widmer, T., Kappenberg, A., Busso, A. A. S., Schnetger, B., & Brumsack, H.-J. (2017). Meltwater as a source of potentially bioavailable iron to Antarctica waters. *Antarctic Science*, *29*(3), 277-291.

Monien, P., Lettmann, K. A., Monien, D., Asendorf, S., Wölfl, A.-C., Lim, C. H., Thal, J., Schnetger, B., & Brumsack, H.-J. (2014). Redox conditions and trace metal cycling in coastal sediments from the maritime Antarctic. *Geochimica et Cosmochimica Acta*, *141*, 26-44.

Nielsdóttir, M. C., Bibby, T. S., Moore, C. M., Hinz, D. J., Sanders, R., Whitehouse, M., Korb, R., & Achterberg, E. P. (2012). Seasonal and spatial dynamics of iron availability in the Scotia Sea. *Marine Chemistry*, *130*, 62-72.

Obata, H., Karatani, H., & Nakayama, E. (1993). Automated determination of iron in seawater by chelating resin concentration and chemiluminescence detection. *Analytical Chemistry*, *65*(11), 1524-1528.

Pereira, P. S., van de Flierdt, T., Hemming, S. R., Hammond, S. J., Kuhn, G., Brachfeld, S., Doherty, C., & Hillenbrand, C.-D. (2018). Geochemical fingerprints of glacially eroded bedrock from West Antarctica: Detrital thermochronology, radiogenic isotope systematics and trace element geochemistry in Late Holocene glacial-marine sediments. *Earth-Science Reviews*, *182*, 204-232.

Poulton, S. W., & Canfield, D. E. (2005). Development of a sequential extraction procedure for iron: implications for iron partitioning in continentally derived particulates. *Chemical Geology*, *214*(3-4), 209-221.

Radic, A., Lacan, F., & Murray, J. W. (2011). Iron isotopes in the seawater of the equatorial Pacific Ocean: New constraints for the oceanic iron cycle. *Earth and Planetary Science Letters*, *306*(1-2), 1-10.

Raiswell, R., & Canfield, D. E. (2012). The iron biogeochemical cycle past and present. *Geochemical perspectives*, *1*(1), 1-2.

Retallick, K., Van Landeghem, K., Fremand, A., Howard, F., Sands, C., Roman-Gonzalez, A., Barnes, D., Jenkins, S., Munoz-Ramirez, C., & James, S. (2021). Seafloor bathymetry of Sheldon Cove, Börgen Bay and Marian Cove, merged and gridded from EM122 multibeam echosounder data collected for the project NE/P003087/1 (2017-2020)(Version 1.0). *Polar Data Centre, Natural Environment Research Council, UK Research & Innovation*.

Rignot, E., Casassa, G., Gogineni, P., Krabill, W., Rivera, A., & Thomas, R. (2004). Accelerated ice discharge from the Antarctic Peninsula following the collapse of Larsen B ice shelf. *Geophysical Research Letters*, *31*(18).

Sands, C. J., Annett, A., Apeland, B., Barnes, D. K. A., Bascur, M., Bruning, P., Costa, M., Dadd, G., De Lecea, A., Ensor, N., Featherstone, A., Flint, G., Goodger, D., Guzzi, A., Howard, F., Hunter, D., Jenkins, S., Kender, S., Lincoln, B., . . . Zwerschke, N. (2019). *JR18003 Cruise Report*. https://www.bodc.ac.uk/resources/inventories/cruise_inventory/report/17247/

Schloss, I., Klöser, H., Ferreyra, G., Mercuri, G., & Pinola, E. (1997). Factors governing phytoplankton and particulate matter variation in Potter Cove, King George island, Antarctica. *Antarctic communities*, 135-141.

Schlosser, C., de La Rocha, C. L., & Croot, P. L. (2011). Effects of iron surface adsorption and sample handling on iron solubility measurements. *Marine Chemistry*, *127*(1-4), 48-55.

Schroth, A. W., Crusius, J., Sholkovitz, E. R., & Bostick, B. C. (2009). Iron solubility driven by speciation in dust sources to the ocean. *Nature Geoscience*, *2*(5), 337-340.

Scourse, J., Barnes, D., Meredith, M., Sands, C., Retallick, K., Munoz Ramirez, C., Roman-Gonzalez, A., Alexandroff, S., Annett, A., Blumenroeder, J., Bull, C., Butler, P., Costa, M., de Lecea, A., Ehmen, T., Falagan Rodriguez, C., Flanagan, O., Flint, G., Fremand, A., . . . Vora, M. (2022). *Impacts of deglaciation on benthic marine ecosystems in Antarctica (ICEBERGS): JR19002 data* NERC EDS British Oceanographic Data Centre NOC. https://doi.org/doi:10.5285/d9633a6c-d27e-30b4-e053-6c86abc07104

Scourse, J. D., Alexandroff, S., Annett, A., Barnes , D. K. A., Blumenroeder , J., Bull , C., Butler, P., Costa, M., De Lecea, A., Ehmen, T., Falagan-Rodriguez, C., Flanagan, O., Flint, G., Frémand , A., Furze, M., Garza, T., Gillun, T., Guzzi, A., Guzman, F., . . . Vora, M. (2020). *JR19002 Cruise Report*. https://www.bodc.ac.uk/resources/inventories/cruise_inventory/report/17557/

Seeberg-Elverfeldt, J., Schlüter, M., Feseker, T., & Kölling, M. (2005). Rhizon sampling of porewaters near the sediment-water interface of aquatic systems. *Limnology and Oceanography: Methods*, *3*(8), 361-371.

Sherrell, R. M., Annett, A. L., Fitzsimmons, J. N., Roccanova, V. J., & Meredith, M. P. (2018). A shallow bathtub ring of local sedimentary iron input maintains the Palmer Deep biological hotspot on the West Antarctic Peninsula shelf. *Philosophical Transactions of the Royal Society A: Mathematical, Physical and Engineering Sciences*, *376*(2122), 20170171. https://doi.org/10.1098/rsta.2017.0171

Shoenfelt, E. M., Sun, J., Winckler, G., Kaplan, M. R., Borunda, A. L., Farrell, K. R., Moreno, P. I., Gaiero, D. M., Recasens, C., Sambrotto, R. N., & Bostick, B. C. (2017). High particulate iron(II) content in glacially sourced dusts enhances productivity of a model diatom. *Science Advances*, *3*(6), e1700314. https://doi.org/10.1126/sciadv.1700314

Slotznick, S., Sperling, E., Tosca, N., Miller, A., Clayton, K., Van Helmond, N., Slomp, C., & Swanson-Hysell, N. (2020). Unraveling the mineralogical complexity of sediment iron speciation using sequential extractions. *Geochemistry, Geophysics, Geosystems*, *21*(2), e2019GC008666.

Stimpfle, J., Koch, F., Ebner, B., Völkner, C., Zitoun, R., Sukekava, C. F., Sander, S. G., Henkel, S., Bundy, R. M., & Ruacho, A. (2026). Glacially derived iron is more bioavailable to Antarctic phytoplankton than other sources. *Communications Earth & Environment*, *7*(1), 89.

Tagliabue, A., Aumont, O., DeAth, R., Dunne, J. P., Dutkiewicz, S., Galbraith, E., Misumi, K., Moore, J. K., Ridgwell, A., & Sherman, E. (2016). How well do global ocean biogeochemistry models simulate dissolved iron distributions? *Global Biogeochemical Cycles*, *30*(2), 149-174.

Taylor, S. R., & McLennan, S. M. (1985). The continental crust: its composition and evolution.

Tian, H.-A., van Manen, M., Bunnell, Z. B., Reichart, G.-J., Conway, T. M., & Middag, R. (2026). Iron isotope constraints on source and transport of sediment-derived dissolved Fe in the Weddell Sea region. *Geochimica et Cosmochimica Acta*.

Tonnard, M., Planquette, H., Bowie, A. R., van Der Merwe, P., Gallinari, M., Desprez de Gésincourt, F., Germain, Y., Gourain, A., Benetti, M., & Reverdin, G. (2020). Dissolved iron in the North Atlantic Ocean and Labrador Sea along the GEOVIDE section (GEOTRACES section GA01). *Biogeosciences*, *17*(4), 917-943.

Ussher, S. J., Achterberg, E. P., Sarthou, G., Laan, P., de Baar, H. J., & Worsfold, P. J. (2010). Distribution of size fractionated dissolved iron in the Canary Basin. *Marine Environmental Research*, *70*(1), 46-55.

Venables, H. J., Clarke, A., & Meredith, M. P. (2013). Wintertime controls on summer stratification and productivity at the western Antarctic Peninsula. *Limnology and Oceanography*, *58*(3), 1035-1047.

Venables, H. J., Meredith, M. P., & Brearley, J. A. (2017). Modification of deep waters in Marguerite Bay, western Antarctic Peninsula, caused by topographic overflows. *Deep Sea Research Part II: Topical Studies in Oceanography*, *139*, 9-17.

Viollier, E., Inglett, P., Hunter, K., Roychoudhury, A., & Van Cappellen, P. (2000). The ferrozine method revisited: Fe (II)/Fe (III) determination in natural waters. *Applied geochemistry*, *15*(6), 785-790.

Von Der Heyden, B. P., Hauser, E. J., Mishra, B., Martinez, G. A., Bowie, A. R., Tyliszczak, T., Mtshali, T. N., Roychoudhury, A. N., & Myneni, S. C. B. (2014). Ubiquitous Presence of Fe(II) in Aquatic Colloids and Its Association with Organic Carbon. *Environmental Science & Technology Letters*, *1*(10), 387-392. https://doi.org/10.1021/ez500164v

Wedepohl, K. H. (1995). The composition of the continental crust. *Geochimica et Cosmochimica Acta*, *59*(7), 1217-1232.

Wyatt, N. J., Birchill, A., Ussher, S., Milne, A., Bouman, H. A., Shoenfelt Troein, E., Pabortsava, K., Wright, A., Flanagan, O., & Bibby, T. S. (2023). Phytoplankton responses to dust addition in the Fe–Mn co-limited eastern Pacific sub-Antarctic differ by source region. *Proceedings of the National Academy of Sciences*, *120*(28), e2220111120.

Zhang, R., John, S. G., Zhang, J., Ren, J., Wu, Y., Zhu, Z., Liu, S., Zhu, X., Marsay, C. M., & Wenger, F. (2015). Transport and reaction of iron and iron stable isotopes in glacial meltwaters on Svalbard near Kongsfjorden: From rivers to estuary to ocean. *Earth and Planetary Science Letters*, *424*, 201-211.